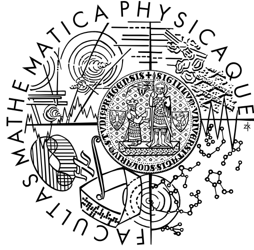

FACULTY
OF MATHEMATICS
AND PHYSICS
Charles University

BACHELOR THESIS

Jakub Strnad

Optical Scanning Profilometer

Department of Chemical Physics and Optics

Supervisor of the bachelor thesis:	prof. RNDr. Petr Němec, Ph.D.
Consultant of the bachelor thesis:	Mgr. Andrej Farkaš
Study programme:	Physics
Study branch:	Physics

Prague 2023

I declare that I carried out this bachelor thesis independently, and only with the cited sources, literature and other professional sources. It has not been used to obtain another or the same degree.

I understand that my work relates to the rights and obligations under the Act No. 121/2000 Sb., the Copyright Act, as amended, in particular the fact that the Charles University has the right to conclude a license agreement on the use of this work as a school work pursuant to Section 60 subsection 1 of the Copyright Act.

In .... date ....

Author's signature

Here, I would like to thank prof. RNDr. Petr Němec, Ph.D., for supervising my work and giving helpful suggestions regarding my thesis. I would like to express my gratitude to Mgr. Andrej Farkaš, who provided invaluable guidance throughout the course of this work. I would also like to thank Ing. Vít Novák, CSc., for coming up with the idea of this device and for supplying the samples for the measurements. Additionally, my gratitude goes to Miroslav Dušek, who constructed the detectors for my device. I would also like to thank the Faculty of Mathematics and Physics of Charles University for allowing me to take this opportunity and write this thesis at the Institute of Physics of the Czech Academy of Sciences. Last but not least, I would like to thank my family and all of my friends for their support, patience and helpful nature.

Title: Optical Scanning Profilometer

Author: Jakub Strnad

Department: Department of Chemical Physics and Optics

Supervisor: prof. RNDr. Petr Němec, Ph.D., Department of Chemical Physics and Optics

Abstract: The focus of this thesis is on the examination of how the uniformity of the grown thin films is influenced by the internal construction of a Molecular Beam Epitaxy (MBE) machine. In order to investigate these effects, a specialized device was constructed, which is capable of measuring the transmissivity and reflectivity of a wide range of films grown on substrates. With the utilization of this device, a 2D map depicting the film's uniformity is generated from the measured data. Valuable insights regarding the characteristics of the molecular beam are derived from this analysis.

Keywords: Molecular Beam Epitaxy Optical Scanning Profilometer Uniformity Asymmetry

Contents

Introduction **3**

1 Theory **4**
1.1 Molecular Beam Epitaxy . . . 4
1.1.1 Vacuum conditions . . . 5
1.1.2 Real Time Monitoring and Control . . . 8
1.1.3 Sources of Atomic and Molecular Beams . . . 9
1.1.4 Real Effusion cell . . . 13
1.2 Laser . . . 14
1.2.1 Principle of Lasers . . . 15
1.2.2 Self-sustained Oscillation . . . 17
1.2.3 Semiconductor Laser . . . 17
1.3 Photodiode Detector . . . 18
1.3.1 Principle of Photodiode . . . 18
1.4 Wave Propagation in Layered Medium . . . 21

2 Construction of Optical Scanning Profilometer **28**
2.1 Construction of Experimental Setup . . . 28
2.1.1 First Floor . . . 29
2.1.2 Second Floor . . . 29
2.1.3 Third Floor . . . 30
2.2 Measuring Process . . . 30
2.2.1 Programming of the Measurement . . . 31
2.2.2 Measurement Devices . . . 32
2.2.3 Spot size measurement . . . 33
2.3 Data Analysis . . . 36
2.3.1 Effects of Interference on Measurements . . . 39

3 Experimental Measurements **40**
3.1 Sapphire Substrate . . . 40
3.1.1 Copper . . . 41
3.1.2 Silver . . . 42
3.1.3 Manganese . . . 44
3.1.4 Arsenic . . . 46
3.1.5 Gallium . . . 47

4 Discussion **50**
4.1 Oxidation and Dust Pollution . . . 50
4.2 Device Improvements . . . 51
4.2.1 Samples on Different Substrates . . . 51
4.2.2 Compactness . . . 51
4.2.3 User Experience . . . 52

Conclusion **53**

Bibliography **54**

List of Figures 56

List of Abbreviations 60

Introduction

Molecular Beam Epitaxy (MBE) is a prevalent effusion technique used for depositing thin films on various substrates. The internal geometry of an MBE machine significantly influences the growth symmetry, ultimately impacting the uniformity and thickness of the films produced.

The primary objective of this thesis is to investigate these asymmetrical effects arising from the MBE machine's internal geometry and the construction of effusion cells on film uniformity. In this thesis, we design and construct a compact, low-cost and modular optical scanning profilometer that is able to measure and analyze a wide range of samples. This device is automated to measure the transmissivity and reflectivity of the films, enabling thorough analysis of these measurements to discern and quantify the quality of the grown films.

The modular design of the device enables the user to change the parameters of the measurement to suit a wide range of samples. The adjustable measuring step capable of reaching 10 μm can be matched with an adjustable laser spot size. Additionally, the laser diode and detectors can be changed if necessary. Currently, a laser diode with a wavelength of 658 nm is being utilized. However, for the purpose of measuring different films on various substrates, the diode operating in the transparent region of the used substrate can be substituted. Alternative detectors can also be easily replaced to cover the broader spectrum than 200 to 1100 nm of our current Si detectors, depending on the situation's requirements.

Furthermore, our device is equipped with a removable 3D-printed sample holder that allows for easy and fast modifications. By adapting and customizing the sample holder, a wide range of sample sizes and types can be accommodated.

The films are analyzed by dividing them into equiuniform surfaces for visual examination. During this assessment, the identification of minimum and maximum intensity values and the calculation of the angle of deposition from the effusion cell are performed. These analyses yield valuable insights into the uniformity and characteristics of the molecular beam, providing additional information about the effects of asymmetry in an MBE.

1. Theory

The first chapter of this thesis is dedicated to the theoretical knowledge of the studied field.

It starts with the description of a Molecular Beam Epitaxy (MBE) technique—the physics behind the manufacturing of thin films and all the used monitoring and ultra-high vacuum equipment inside an MBE machine.

In the second section, the physical principles and typical types of lasers are discussed. The semiconductor laser is explained in more detail.

The third section depicts the working principles of a photodiode detector.

Lastly, in the fourth section, the propagation of an electromagnetic wave in a layered dielectric and conducting medium is described.

1.1 Molecular Beam Epitaxy

Molecular Beam Epitaxy (MBE) is a versatile technique employed for growing thin epitaxial structures of semiconductors, metals, or insulators with exceptional precision and control [1]. This layer-by-layer technique is done in an Ultra-High Vacuum (UHV). The difference between MBE and other epitaxial techniques is the use of UHV, which allows the use of in-situ techniques such as Auger Electron Spectroscopy (AES), Reflection High Energy Electron Diffraction (RHEED), or ellipsometry. This eliminates most guesswork during the growth of the thin film and enables precise control of the doping, composition, and interfaces on a sub-nanometer scale. However, the uniformity in thickness and the design of the films grown by MBE relies on the uniformity of molecular beam fluxes and the geometric relationship between the source configuration and the substrate [1].

The mechanical structure of an MBE, as shown schematically in Fig. 1.1, consists of three heat-resistive stainless steel UHV chambers: the entry/exit chamber, called load lock, the growth chamber, and the preparation (buffer) chamber, which connects the two [2]. These chambers are divided by UHV swing gate valves. Heat-resistant materials like molybdenum are used to construct the heating block, upon which the substrates are positioned. Transfer rods facilitate the movement of the substrates between chambers. The separation of the three chambers allows to maintain constant UHV in the growth chamber. The essential equipment inside the growth chamber is the UHV pumping system, effusion cells, a heating block equipped with a thermocouple capable of azimuthal rotation for lateral conformity, ionization gauge for beam flux and vacuum monitoring and in-situ monitoring apparatus such as RHEED. Pumping down, preheating, and storing the substrates are all carried out in the entry/exit chamber. All of the other chambers are kept in a constant vacuum.

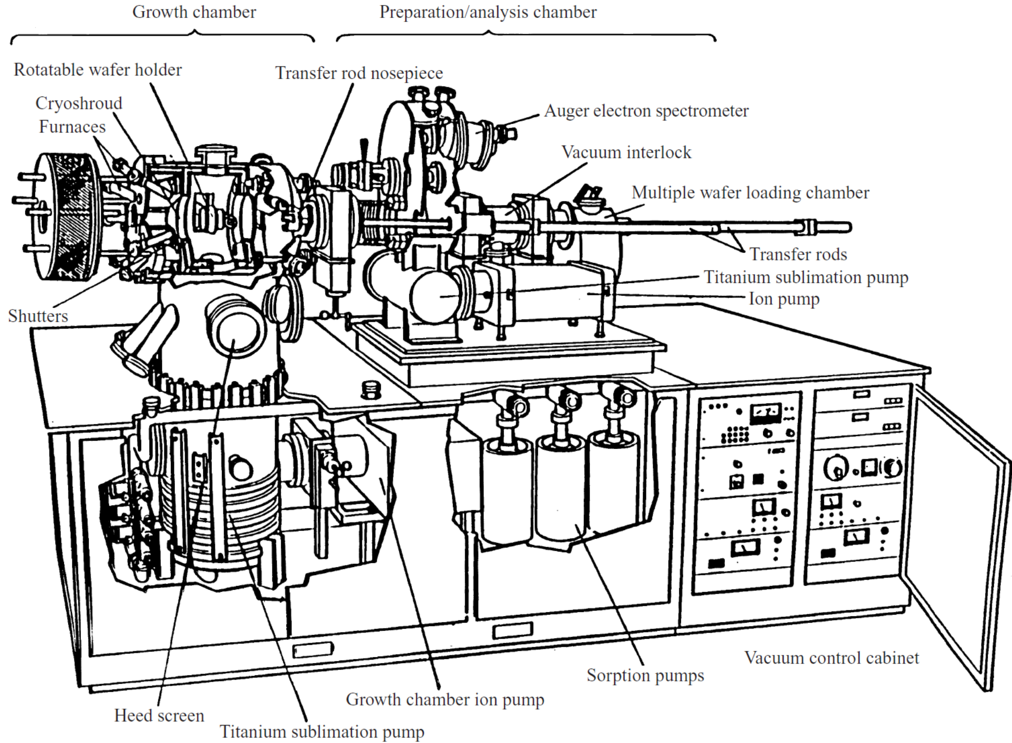

Figure 1.1: Schematic representation of the key components within an MBE growth machine. Adapted from [2].

1.1.1 Vacuum conditions

Usually, two types of vacuums are differentiated, the High Vacuum (HV), with residual pressure p, $1,33 \times 10^{-1}$ Pa $\geq p \geq 1,33 \times 10^{-7}$ Pa and UHV, with residual pressure less than $1,33 \times 10^{-7}$ Pa [1]. In the commonly used MBE chambers, the approximate distance between the effusion cells and the substrate is about $0,2$ m. If the pressure is not low enough, the molecules may collide with residual gas molecules, leading to molecular beam flux degradation. The maximum permissible value for the residual gas pressure $p_{g,max}$, for growth of GaAs was estimated to be $p_{g,max} = 7,7 \times 10^{-2}$ Pa [1]. It is conspicuous that the pressure needed for the integrity of the beam is in the HV range. However, the low growth rate of conventional MBE techniques (about 1 μm/h [1]) introduces potential layer contamination by the deposition of the residual gas on the substrate, which, together with the requirements for the high layer purity, induces much stricter conditions for the total pressure. To ensure the growth of a suitably clean epilayer, a crucial condition is that the time interval $t_1(v)$ required for the deposition of one monolayer of contaminants on the substrate surface from the residual gas present in the growth chamber should be one hundred thousand times greater than the time interval $t_1(b)$ needed for the deposition of a one-monolayer film from the molecular beams. [1]

$$t_1(b) = 10^{-5} t_1(v) \tag{1.1}$$

For this condition and the rate of growth (1 μm/h), it was estimated that the maximal pressure $p_{i,max}$ in that vacuum chamber must be [1]:

$p_{i,max} = 1,7 \times 10^{-9}$ Pa, which indicates that the low growth rate MBE technique should be executed in the UHV.

To achieve necessary UHV conditions, a combination of different pumps is being used. The pumping of the load lock is done by a scroll pump connected to the preparation chamber by an all-metal gate valve. The preparation chamber is pumped by three ion-getter pumps. Then, a liquid nitrogen-cooled cryo pump is used to achieve the UHV in the growth chamber.

Scroll pump

To prevent the substrate's contamination, a "dry" scroll pump is preferred. A scroll pump is comprised of several key components, such as a vacuum housing containing two spiral-shaped scrolls. Within the scroll assembly, there is a stationary spiral and a movable spiral called the orbiter, which eccentrically moves without rotation. Gas enters the open end of the spirals, and as the orbiter moves, it passively captures and conveys the gas between the scrolls toward the center. The gas undergoes compression and its volume reduces as it is passively "squeezed and transported" between the spirals. Ultimately, the compressed gas is discharged at pressure through a non-return valve positioned at the center of the housing. The pumping speed of the scroll pump is 250 l/s and can achieve a vacuum of 5×10^{-7} Pa. The basic principle of the scroll pump is shown in Fig. 1.2

Figure 1.2: Gas path in scroll pump. Adapted from [3].

Ion-getter pumps

Ion-Getter Pump (IGP) are a type of sorption pump based on the Penning cell [4], composed of an anode typically made of stainless steel and two opposite titanium cathodes, which have the ability to capture electrons through the combination of electric and magnetic fields. The objective of the Penning cell is to ionize a significant amount of the gas, causing it to be attracted toward the cathodes. In our MBE, there are three of these pumps, each with a pumping speed of 400 l/s, and can obtain the pressure of 1×10^{-8} Pa. In Fig. 1.3 is shown the basic structure of an IGP.

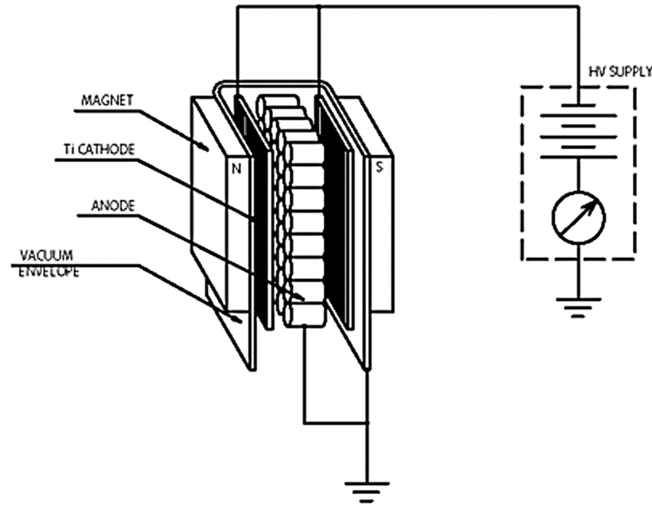

Figure 1.3: Schematic representation of ion-getter pump.

Cryopump

A cryopump is used to achieve the working pressure of 5×10^{-10} Pa in the growth chamber. A cryopump is a type of vacuum pump that passively captures and condenses gases and vapors by exposing them to a cold surface. It has two stages. In the first stage, the focus is primarily on removing moisture, while in the second stage, molecules such as N_2, O_2, Ar, and H_2 are further expelled by additional cooling (10-12 K) to achieve a higher level of vacuum. However, the lightest gases such as hydrogen, helium, and neon cannot be condensed at 20 K alone. Special porous materials are used as adsorbents to effectively capture these gases, instead of relying solely on condensation. By cooling the adsorbent below 20 K, these gases are efficiently adsorbed, enabling the attainment of ultra-high vacuum by a cryopump.

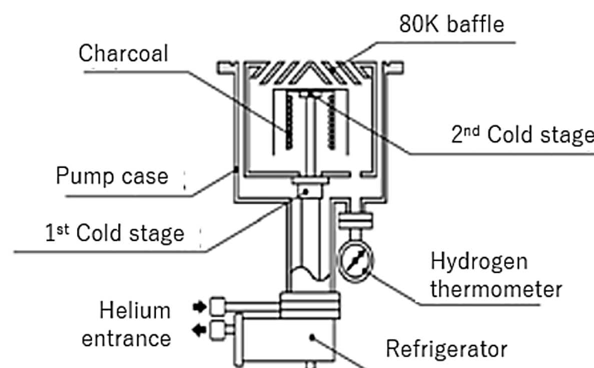

Figure 1.4: Basic structure of a cryopump.

1.1.2 Real Time Monitoring and Control

In the UHV environment of MBE, it is possible to utilize analytical equipment, such as *Modulated Beam Mass Spectroscopy (MBMS)*, directly inside the growth chamber. MBMS can be employed to identify desorbed species, determine desorption rates, measure sticking coefficients, analyze the order of chemical reactions, evaluate thermal accommodation coefficients, assess surface lifetimes, and determine surface binding energies [5].

During the growth process, *Desorption mass spectroscopy* is commonly utilized to monitor desorbed species. It enables the monitoring and control of growth rate and composition within a closed-loop feedback system, even when substrate rotation is involved [6].

Reflection High Energy Electron Diffraction (RHEED) is used for the observation of oxide desorption, surface reconstruction, surface coverage, and the establishment of the phase diagram. Additionally, surface steps, domains, disorder, surface smoothing, and the effects associated with surface misorientation can be monitored. [7].

The observation of the time evolution of the growth of each monolayer, roughening and smoothing during monolayer growth, surface mobility of adsorbed atoms and molecules, as well as the growth mechanism and kinetics, is facilitated through the utilization of *RHEED intensity oscillations* [8].

The chemical identification of surface species, particularly at different stages of oxide desorption, is achieved through the use of *Auger Electron Spectroscopy (AES)*. AES proves to be a beneficial technique for the development of optimal surface preparation recipes for new substrate materials. [2].

Powerful and novel techniques for atomistic observation and determination of surface reconstruction as a function of growth, surface preparation, and growth conditions are provided by *Scanning tunneling microscopy and atomic force spectroscopy* [9].

Optical characterization techniques like ellipsometry and band-edge thermometry are used to monitor and control real-time substrate temperature, growth rate, thickness, composition, and surface morphology.

Reflection High Energy Electron Diffraction (RHEED)

In the deposition chamber of an MBE machine, there are usually fitted structural monitoring facilities such as RHEED. Information on the structural integrity of the substrate and growing film in the normal growth position is provided by the RHEED system. The diffracted and reflected beams are subsequently displayed using a fluorescent phosphorus screen within the deposition chamber. The diffraction pattern is then processed and evaluated in a specially designed optoelectronic system.

The experimental geometry of RHEED is shown in Fig. 1.5. Through the utilization of RHEED, simultaneous measurement of electron diffraction and molecular beam deposition is enabled. The de Broglie wavelength of the electron is significantly smaller compared to the monolayer thickness of approximately 3Å and the surface inter-atomic thickness. This makes RHEED an ideal technique for controlling the structural integrity of the growing surface on the atomic scale, both laterally and vertically.[10]

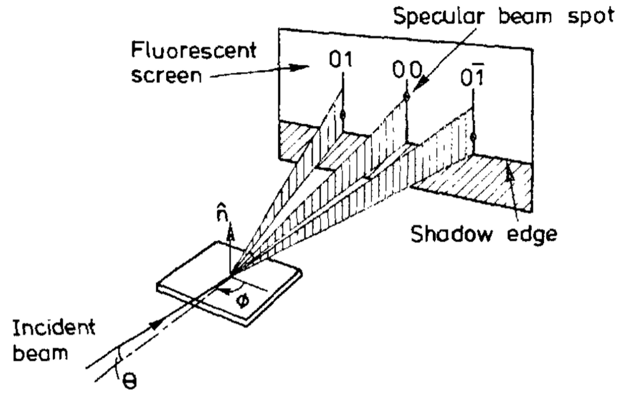

Figure 1.5: Schematic diagram illustrating the RHEED geometry. It showcases the incident beam positioned at an angle θ relative to the surface plane, along with the azimuthal angle ϕ. The elongated spots within the diagram represent the points of intersection between the Ewald sphere and the 01, 00, and $0\bar{1}$ rods. Adapted from [11].

Band-edge Thermometry

Band-Edge Thermometry (BET), otherwise known as absorption band-edge spectroscopy, is a wide-used, very precise method for measuring the substrate temperature during MBE growth[12].

The base principle of this method is that many substrates are essentially transparent in the Infrared (IR) range of the spectrum. However, with the rising temperature, the light begins to be absorbed by the substrate, and due to thermal expansion, the absorption edge becomes shifted. The light that is transmitted by the substrate is measured and the temperature can be calculated from the position of the transmitted light absorption edge.

1.1.3 Sources of Atomic and Molecular Beams

The utilization of specialized beam sources is crucial to ensure the critical factors of growth uniformity and reproducibility. The composition and thickness of films achieved through MBE are primarily influenced by the uniformity of molecular beams across the substrate. The distribution of molecular beam patterns relies on the angular flux distribution from each source within the system and the geometry of the "source-substrate" configuration. Optimal uniformity of beam patterns is attained by maintaining a significant spacing between the source and substrate, while flux distributions at the source orifices need to be isotropic in the space angle occupied by the substrate [13]. On the other hand, the reproducibility of the growth process is dependent upon the long-term stability of beam fluxes and the short-term variations during the opening and closing of shutters. Another factor that determines the structure of the film created in the shape of the base material used for MBE growth. This thesis will discuss only the source-related parameters that influence the MBE process.

The Effusion Process and the Ideal Effusion Cell

The effusion process is classified within the realm of evaporation phenomena and is described by evaporation theory. A systematic investigation of evaporation was first conducted by *Hertz* in 1882, focusing on mercury under reduced air pressure conditions. It was discovered that there exists a maximum evaporation rate, even when the heat supply is unlimited. The theoretical maximum evaporation rates are achieved when the number of molecules leaving the surface equals the required number of molecules to maintain the equilibrium pressure p_{eq}, with none of them rebounding [14]. This implies the necessity of maintaining a hydrostatic pressure of $p = 0$. Consequently, based on these considerations, the number of molecules dN_e evaporating from a surface A_e during a time interval dt can be expressed as follows [1]:

$$\frac{dN_e}{A_e dt} = (p_{eq} - p)\sqrt{\frac{N_A}{2\pi M k_B T}}\ [m^{-2}s^{-1}], \tag{1.2}$$

where the molecular weight of the evaporating molecules is denoted as M, while p_{eq} represents the equilibrium pressure. Hydrostatic pressure is represented by p, and the Boltzmann and Avogadro constants are denoted as k_B and N_A, respectively. However, when Hertz conducted measurements, the maximum rates observed were found to be ten times lower than the theoretical maximum rates. This discrepancy arises because a portion of the molecules colliding with the evaporating surface is reflected back into the gas instead of being incorporated into the liquid. *Knudsen* addressed this issue in 1915 by modifying the equation and introducing the evaporation coefficient a_v. This coefficient is defined as the ratio of the observed evaporation rate in a vacuum to the theoretically possible rate as described by Equation (1.2). As a result, the most comprehensive form of the evaporation rate equation is now expressed as [1]

$$\frac{dN_e}{A_e dt} = a_v(p_{eq} - p)\sqrt{\frac{N_A}{2\pi M k_B T}}\ [m^{-2}s^{-1}], \tag{1.3}$$

which is commonly known as the Hertz-Knudsen equation.

Later an alternative evaporation technique was developed by *Langmuir* in 1913 [15] by evaporating from free solid surfaces. A modification of this technique of solid surfaces was established by *Knudsen* [16] and is associated with his name. Evaporation takes place in this technique through effusion from an isothermal enclosure equipped with a small orifice, which is known as a Knudsen cell. Because the orifice is small compared to the evaporating surface within the chamber, pressure equilibrium is maintained. For this, the ratio of the diameter of the orifice and the mean free path of the gas must be less than one to ten, and the particles cannot be scattered or adsorbed by the orifice wall. Under the given conditions, the orifice is regarded as an evaporating surface with the evaporator pressure p_{qe} and an evaporation coefficient of $a_v = 1$. If A_e represents the area of the orifice, the total number of molecules effusing from the Knudsen cell into the vacuum per unit time, referred to as the real effusion rate $\mathit{\Gamma}_e$, can be calculated as [1]

$$\mathit{\Gamma}_e \equiv \frac{dN_e}{dt} = A_e(p_{eq} - p_v)\sqrt{\frac{N_A}{2\pi M k_B T}}\ [\text{molecules s}^{-1}], \tag{1.4}$$

The pressure in the vacuum reservoir, to which the molecules effuse from the cell orifice, is represented by p_v. The Knudsen equation is often written in the form [1]

$$\mathit{\Gamma}_e \equiv 3,51 \times 10^{22} \frac{pA_e}{\sqrt{MT}} \text{ [molecules s}^{-1}\text{]}, \tag{1.5}$$

p representing the pressure of the effusion cell in [Torrs], and all other quantities are in Centimetre–gram–second system (CGS) units.

The cosine Law of Effusion

In an ideal Knudsen cell, the vapor of the charged material and the condensed phase are maintained in thermodynamic equilibrium. The effusion aperture of the cell is a small orifice located within an infinitesimally thin cell lid. The gas reservoirs inside and outside the cell are sufficiently large, ensuring that molecules are more likely to interact with each other rather than with the cell walls. As depicted in Fig. 1.6, the particles of the charge vapor exit the cell into the UHV environment in all directions, surrounded by a hemisphere centered at the orifice. When a single molecule m moves along a straight line in the direction θ of the cell orifice, it passes through without altering its trajectory due to the assumption that the orifice wall has an infinitesimally thin thickness ($L_0 \approx 0$). The differential angular effusion rate $d\mathit{\Gamma}_\vartheta$ from the orifice area A_e into the vacuum in directions between $\vartheta + d\vartheta$ is directly proportional to [1]:

1. The surface of the orifice seen by the molecule

$$d\mathit{\Gamma}_\vartheta \sim A_e \cos \vartheta.$$

2. The unit area of the orifice is entered by a number of molecules in unit time

$$d\mathit{\Gamma}_\vartheta \sim \frac{\mathit{\Gamma}_e}{A_e} = 3,51 \times 10^{22} \frac{p}{\sqrt{MT}}.$$

3. The probability P of a molecule m entering the orifice within the range of directions between ϑ and $\vartheta + d\vartheta$ can be determined. This probability is directly proportional to the solid angle $d\omega$ at dS that is subtended by these directions. The solid angle element $d\omega$ is measured by the area on a sphere with a radius r (as shown in Fig. 1.6) corresponding to the circular zone between the angles $\vartheta + d\vartheta$. It can be expressed as follows:

$$d\omega = \frac{dS}{r^2} \sin \vartheta d\vartheta.$$

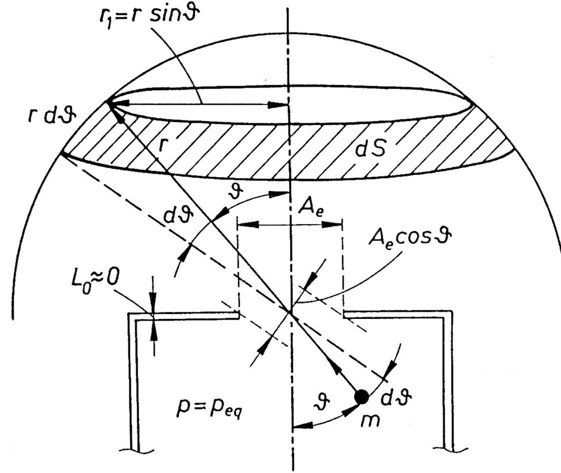

Figure 1.6: A schematic illustration depicting the upper section of an ideal Knudsen effusion cell. The diagram highlights the geometric quantities that are relevant to the calculations of flux distribution. Adapted from [1].

The probability of a molecule leaving the cell into an angle ϑ that lies between ϑ and $\vartheta + d\vartheta$ is [1]

$$P = \frac{d\omega}{2\pi} = \sin\vartheta d\vartheta. \tag{1.6}$$

Thus $d\mathit{\Gamma}_\vartheta \sim \sin\vartheta d\vartheta$.

The formula expressing the differential angular effusion rate $d\mathit{\Gamma}_\vartheta$ of molecules escaping from the cell orifice [1]

$$d\mathit{\Gamma}_\vartheta = (C_0 A_e \cos\vartheta)\left[\left(\frac{\mathit{\Gamma}_e}{A_e}\right)\sin\vartheta d\vartheta\right], \tag{1.7}$$

given that $0 \leq \vartheta \leq \frac{\pi}{2}$ and the total effusion rate of the molecules is equal to $\mathit{\Gamma}_e$, the proportionality constant C_0 can be calculated (1.5). Therefore [1]

$$\mathit{\Gamma}_e = \int_0^{\pi/2} d\mathit{\Gamma}_\vartheta = \int_0^{\pi/2} C_0 \mathit{\Gamma}_e \cos\vartheta \sin\vartheta \, d\vartheta = \frac{C_0 \mathit{\Gamma}_e}{2}, \tag{1.8}$$

this implies that the proportionality constant C_0 is equal to 2.

Now rewriting the formula (1.7) as [1]

$$d\mathit{\Gamma}_\vartheta = \frac{\mathit{\Gamma}_e}{\pi}\cos\vartheta d\omega. \tag{1.9}$$

This equation (1.9) is usually referred to as the cosine law of emission. By utilizing equations (1.5) and (1.9), along with the Knudsen effusion equation and the cosine law of effusion, the impingement rate I_A of the molecular beam at point A of the substrate mounted axially in front of the effusion cell (Fig. 1.7a) can be calculated. The angular effusion rate for $\vartheta = 0$ per unit substrate area $dS = d\omega r_A^2$ around point A determines this impingement rate. [1]:

$$I_A \equiv \left.\frac{d\mathit{\Gamma}_\vartheta}{dS}\right|_{\vartheta=0} = \frac{\mathit{\Gamma}_e}{\pi r_A^2} = 1,118 \times 10^{22} \frac{pA_e}{r_A^2\sqrt{MT}} \ [\text{molecules cm}^{-2}\text{s}^{-1}], \tag{1.10}$$

where p is expressed in [Torrs] and other quantities in CGS units.

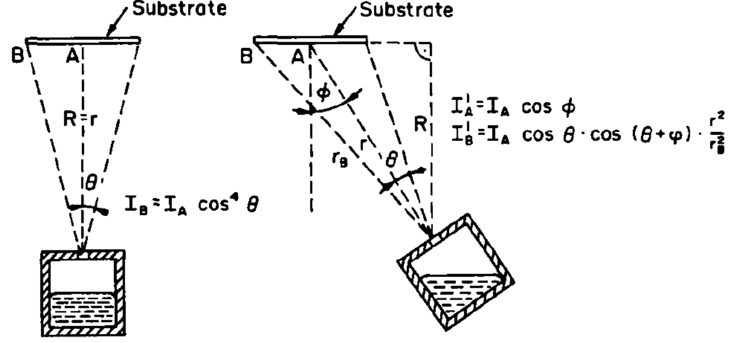

Figure 1.7: Molecular flux distribution across axially (a) and non-axially (b) mounted substrates, in relation to the effusion cell orifice in the MBE chamber. Adapted from [17].

The flux at the edge point B is determined by $I_B = d\Gamma_\vartheta / dS(\vartheta)$, where $dS(\vartheta)$ is the surface element around point B defined as $dS(\vartheta) = [(d\omega r_A^2)/\cos\vartheta] \cdot (r_B^2/r_A^2)$ [1]. Therefore, I_B can be expressed in the following form [1]

$$I_B = \frac{\Gamma_e \cos^2\vartheta}{\pi r_A^2} \cdot \frac{r_A^2}{r_B^2} = I_A \cos^4\vartheta. \tag{1.11}$$

It is possible to derive the impingement rate from a source that is tilted by an angle ϕ from the perpendicular substrate axis (Fig. 1.7) in a similar manner [1]:

$$I'_A = I_A \cos(\phi). \tag{1.12}$$

$$I'_B = I_A \frac{r_A^2}{r_B^2} \cos\vartheta \cos(\vartheta + \phi). \tag{1.13}$$

1.1.4 Real Effusion cell

However, in MBE machines, effusion sources with larger orifices are used to produce a reasonable flux rate at lower temperatures than in the ideal Knudsen cell. Because of this larger opening inside the crucible, there is no longer a thermodynamical equilibrium, which must be considered while calculating the flux distribution of the real effusion cell. Simulations of the real effusion cell using the Monte Carlo method were done by Humenberger and Sitter [18].

The simulation results and the most critical information obtained from the calculations are presented in Fig. 1.8. In Figure 1.8b, the relative density of particles crossing the exit plane of the source for different equilibrium vapor pressures is shown. It is observed that the structure of the molecular flux is minimally affected by the vapor pressure. Figure 1.8a illustrates the impingement rate onto a plane situated at a distance L/R. The significant dip in the graph was observed only for a tube with $L/R = 3$; this dip was not observed for larger ratios. This indicates that the drop reflects the geometrical properties of the effusion cell.

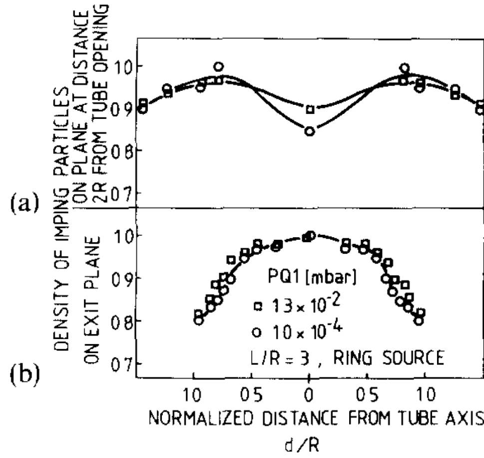

Figure 1.8: Density of particles crossing the exit of the hot-wall tube (a) and density of particles impinging on a plane positioned at a distance L/R above the tube opening(b). Adapted from [18].

It can be seen that the density of particles gradually decreases starting from the center to the edge, which corresponds with the experimental investigation done by Gericke [19] on the cylindrical and conical effusion sources. The results are shown in Fig. 1.9.

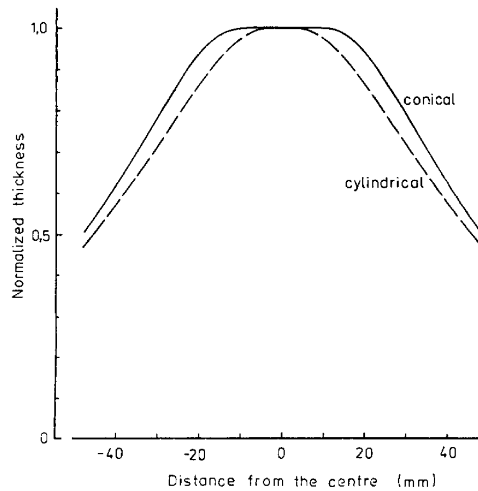

Figure 1.9: The thickness distributions from the cylindrical and conical crucibles under the conditions of $T = 630°C$ and $L/R = 2$. Adapted from [19].

These global defects created by the inhomogeneity of the molecular flux are what we will investigate in the practical part of this thesis.

1.2 Laser

The acronym "Laser" stands for Light Amplification by Stimulated Emission of Radiation. As implied by its name, the crucial aspect of lasers is stimulated emission, a process first introduced by Einstein in 1917. However, the real-world application of this theory did not occur until more than 40 years later.

1.2.1 Principle of Lasers

A working principle of lasers can be best shown by imagining the interaction between electromagnetic (EM) waves and a hypothetical two-energy-layer atomic system. This section elucidates the physical principles of laser technology.

Absorption and Emission

There are three basic processes through which matter can interact with EM radiation, as described by the reference [20]: (1) absorption, (2) spontaneous emission, and (3) stimulated emission. Fig. 1.10 presents the illustration of these processes using hypothetical atoms featuring two energy levels: E_1 (lower level) and E_2 (upper level). The population densities in these levels are denoted as N_1 and N_2 respectively. The interaction between the atoms and a monochromatic, collimated light beam with an angular frequency $\omega = (E_2 - E_1)/\hbar$ can occur in three different ways.

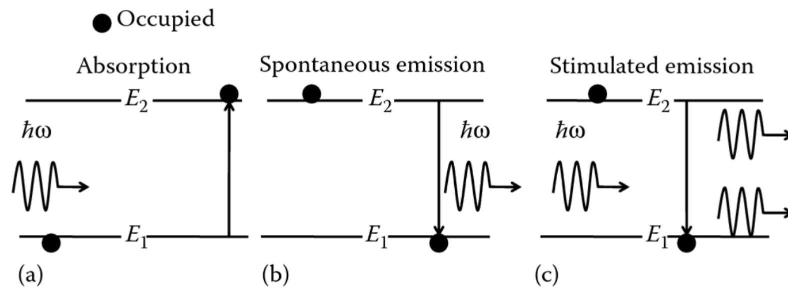

Figure 1.10: The interaction of radiation with a two-level atomic system with three fundamental processes: (a) absorption, (b) spontaneous emission, and (c) stimulated emission. Each process represented by a diagram where the left half depicts the initial state of occupancy of a level, and the right half represents the state of occupancy after the process. Adapted from [20].

The process of *Absorption* is experienced by all materials under normal conditions. In Figure 1.10a, this process is illustrated, where an electron is transferred from the lower energy level to the upper level by absorbing a photon of energy $\hbar\omega = E_2 - E_1$. The incident light's intensity is decreased as a result of absorption, while the polarization and direction of the light remain unchanged. The rate of absorption can be determined by [20]

$$\frac{dN_1(t)}{dt} = -B_{12}N_1\rho(\omega) = -\frac{dN_2(t)}{dt}, \tag{1.14}$$

where the rate of absorption is determined by the Einstein B-coefficient, denoted as B_{12}, and the energy density of the incident photon flux, represented by ρ.

The process of *Spontaneous Emission* involves the spontaneous transition of an atom from the upper energy level to the lower energy level, resulting in the emission of a photon with energy $\hbar\omega$. This process is depicted in Figure 1.10b. The direction in which the emitted radiation is propagated and its polarization is arbitrary. The corresponding rate equation is [20]

$$\frac{dN_1(t)}{dt} = -A_{21}N_2(t) = -\frac{dN_2(t)}{dt}, \tag{1.15}$$

where A_{21} is called Einstein A-coefficient and is related to the spontaneous emission lifetime by $\tau = (A_{21})^{-1}$.

Stimulated Emission is a process when the incident photon induces the atom to make a downward transition from the upper to the lower level, as shown in Figure 1.10c. The energy released is in the form of a photon, which has the same phase, polarization, frequency, and direction of propagation as the incident photon causing the transition. The corresponding rate equation is [20]

$$\frac{dN_2(t)}{dt} = -B_{21}N_2\rho(\omega) = -\frac{dN_1(t)}{dt}, \tag{1.16}$$

where B_{21} is the Einstein B-coefficient for stimulated emission.

Absorption and Emission Rates

The rates of spontaneous emission, stimulated emission, and absorption from equations (1.14) through (1.16) may be written as [20]

$$R_{\text{spon}} = A_{21}N_2,\ R_{\text{stim}} = B_{21}N_2\rho(\omega),\ \text{and}\ R_{\text{abs}} = B_{12}N_1\rho(\omega). \tag{1.17}$$

In thermal equilibrium, atomic densities obey Boltzmann statistics, and therefore [20]

$$\frac{N_2}{N_1} = \exp\left(-\frac{E_2 - E_1}{k_BT}\right) = \exp\left(-\frac{\hbar\omega}{k_BT}\right), \tag{1.18}$$

where k_B represents the Boltzmann constant and T represents the absolute temperature. The rates for upward and downward transitions under a steady state should be equal, leading to [20]

$$A_{21}N_2 + B_{21}N_2\rho(\omega) = B12N_1\rho(\omega). \tag{1.19}$$

Combining together equations (1.18) and (1.19) we get the spectral density as

$$\rho(\omega) = \frac{\frac{A_{21}}{B_{21}}}{\frac{B_{12}}{B_{21}} \cdot \exp\left(\frac{\hbar\omega}{k_BT}\right) - 1}. \tag{1.20}$$

In thermal equilibrium, the radiation spectral density must be equal to that of the blackbody radiation, which is determined by the Planck formula [20]

$$\rho_{BB} = \frac{2\hbar\omega^3}{\pi c^3}\frac{1}{\exp\left(\frac{\hbar\omega}{k_BT}\right) - 1}. \tag{1.21}$$

Comparing the equations (1.20) and (1.21) we get relations

$$A_{21} = \frac{2\hbar\omega^3}{\pi c^3}B_{21}\ \text{and}\ B_{12} = B_{21} \tag{1.22}$$

Therefore the ratio of stimulated to spontaneous emission rates is

$$\frac{R_{\text{stim}}}{R_{\text{spon}}} = \left[\exp\left(\frac{\hbar\omega}{k_BT}\right) - 1\right]^{-1}, \tag{1.23}$$

In the visible and infrared region ($\hbar\omega \sim 1$ eV), it is shown by Equation (1.23) that near room temperature ($k_B T \approx 25$ meV), spontaneous emission surpasses stimulated emission. Additionally, it is indicated by equations (1.17) and (1.23) that $R_{\text{stim}} > R_{\text{abs}}$ only when $N_2 > N_1$. This condition is fulfilled when the system is operated away from thermal equilibrium. This state of the system where the requirement for laser operation is achieved is known as a population inversion.

1.2.2 Self-sustained Oscillation

Although the primary phenomenon of interest is light amplification, self-sustained oscillation is commonly supported by laser devices. In order to transform an amplifying medium into an oscillator, the introduction of positive feedback becomes necessary. The fundamental structure of most lasers comprises three components: (1) *a gain medium*, (2) *a pump*, and (3) *a mechanism to provide feedback*. The provision of feedback is typically accomplished through a Fabry-Perot resonator, which is composed of two plane-parallel mirrors, as depicted in Figure 1.11. A standing wave pattern is formed by the electromagnetic (EM) wave that reflects from the end mirrors. The distance L between the two mirrors corresponds to an integral multiple of half wavelengths of the EM field. One mirror possesses a reflectivity of 100%, while the other mirror exhibits a lower reflection, enabling a portion of the light to be transmitted through it.

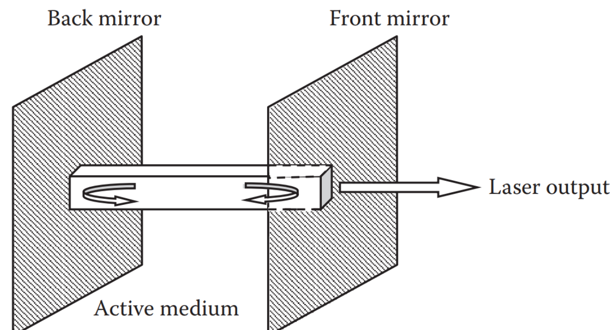

Figure 1.11: The EM field distribution of three longitudinal modes within a Fabry-Perot resonator. Adapted from [20].

The development of lasers has been a significant milestone in the history of science and technology, providing numerous practical applications in fields ranging from communications to manufacturing. The unique properties of lasers, such as high coherence, monochromaticity, and directionality, make them an ideal tool for many applications.

In this chapter, we will focus on the semiconductor laser, a particular type of laser that has become increasingly important in recent years. Semiconductor lasers, also known as diode lasers, have played a vital role in many applications, including data storage, printing, and sensing.

1.2.3 Semiconductor Laser

Numerous classifications of lasers exist, with gas, chemical, dye, metal-vapor, solid-state, and semiconductor lasers being among the most prevalent. As one

of the most pervasive and quintessential coherent light sources available today, an indispensable role in many optical systems, particularly in communication, storage, sensing, and metrological applications is played by the semiconductor laser. In our study, the properties of semiconductor laser are utilized.

Semiconductor lasers are based on semiconductor gain media. The choice of material depends on the desired wavelength and other properties, such as modulation speed. The basic principle of a semiconductor diode laser is similar to that of a diode. Essentially, a diode is a two-layer semiconductor, one layer known as p-type (majority of holes) and the other layer n-type (with more electrons). Putting them together, a p-n junction is formed. In an ordinary diode, the p-n junction works like a barrier that allows the flow of electrons in only one direction (forward-biased operation). As electrons flow across the barrier, they combine with holes and give out energy in the form of phonons that dissipate into the crystal. In a laser diode similar process happens, but the energy is given out in the form of photons. Electrons injected by an electric circuit combine with holes to produce photons, which interact with more electrons that help to make more photons by stimulated emission.

1.3 Photodiode Detector

The quantification of light intensity through a photodiode detector is enabled by the intrinsic properties of a photodiode. An electrical current is generated by this photosensitive semiconductor diode when it is exposed to light. Specifically, the conversion of photons of light into electric charge carriers within the semiconductor precipitates this phenomenon. It is worth noting that even in the absence of a light source, a small electrical current is also generated. An increase in the absorption area of the photodiode leads to an increase in the absorption efficiency of light and the response time, the time taken to produce the intensity. Notably, the illuminating light radiation determines the electrical properties of the photodiode.

1.3.1 Principle of Photodiode

A photodiode is a planar diode constructed so that light can reach the p-n junction. If the p-n junction is not illuminated, the photodiode has the same Volt-Ampere(V-A) characteristic as a standard diode.

In *Photovoltaic* (PV) mode, the excitation of electrons to a higher energy state occurs through the illumination of the semiconductor material of the photodiode. As a result, electrons gain mobility and vacancies (holes) are left behind. The cathode attracts the movement of electrons, while the anode attracts the movement of holes. Consequently, a voltage is established between the two components. This process takes place regardless of the presence of incident light. The small current generated in the absence of light is known as dark current.

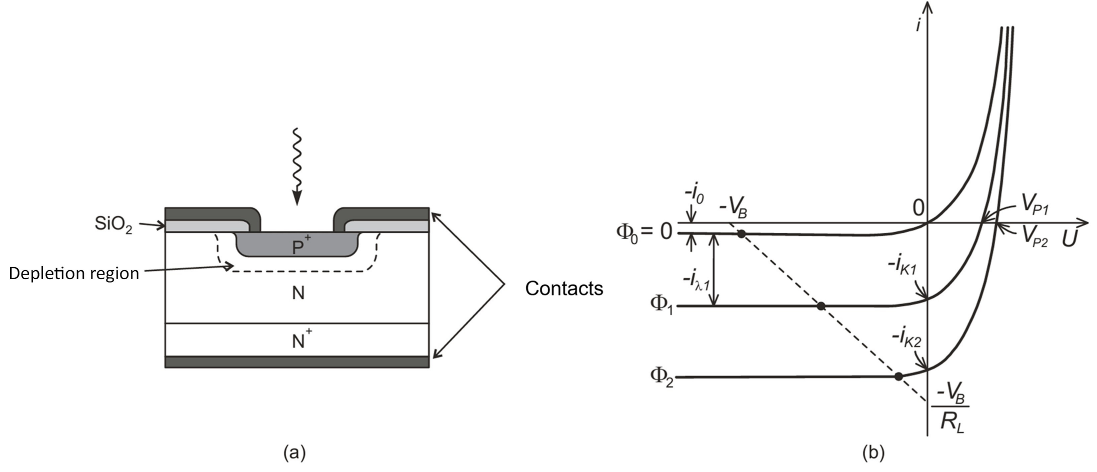

Figure 1.12: (a) basic Si photodiode structure (b) V-A characteristic of a photodiode, Φ_0, Φ_1 and Φ_2 being the photon fluxes, i_0 the dark current, i_λ the photocurrent, $i_{k1;2}$ the reverse saturation current and $V_{P1;2}$ the output voltage. Adapted from [21].

In *Photoconductive* (PC) mode, pairs of electrons and holes are created in the semiconductor material when light strikes the photodiode. Electrons and holes, created by the incoming light, are sucked to the cathode and anode respectively due to the applied bias voltage. As a result, small current flows through the photodiode that can be regulated by the photon flux (Φ_0, Φ_1, Φ_2) (Fig. 1.12). In this mode, the photodiode reacts quickly to the changes in the flux, in the order of $10^{-9} - 10^{-6}$ s. The principle is illustrated in Figure 1.13. The EM radiation generates current J_λ, from which one part J_d flows through the diode and the currents J_{Sh} and J_C through the resistor and capacitor. If we omit these two currents, we get the current J of the outer circuit [21]

$$J = -(J_\lambda - J_d) = -J_\lambda + J_0 \left[\exp\left(\frac{eU}{k_B T} \right) - 1 \right], \tag{1.24}$$

where the total current going through the diode is $J_d = J_0 \left[\exp\left(\frac{eU}{k_B T} \right) - 1 \right]$, J_0 is the dark current, e is the elementary charge.

In the PV mode in the space charge area, the region around the p-n junction where all the charged particles remain, the incoming light generates electron-hole (e-h) pairs. The result is that the size of the electric field increases, which creates the photovoltage V_p. The advantage of the PV mode is that there is no need for a power source. However, the response time is longer in the range of μs.

If there is a large enough applied electric field in the diode in the PC mode, we get a linear increase in the current.

$$J = -(J_\lambda - J_0). \tag{1.25}$$

In the space charge area, the e-h pairs split and are sucked out by the electric field to the electrodes. If there are no impurities that can capture or scatter the generated electrons, there is no reduction of the photocurrent. In an ideal situation without losses, we get

$$J_\lambda = \frac{e\eta P_\lambda z}{h\nu} = \frac{e\eta P_\lambda z}{hc} \lambda. \tag{1.26}$$

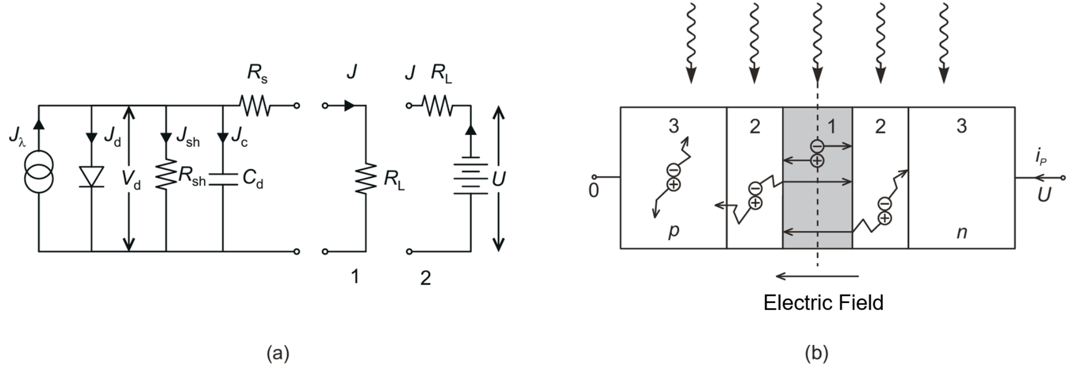

Figure 1.13: (a) Schematic of a photodiode: (a): two possible connections PV mode (1) and PC mode (2). J_λ current generated by the incident light, R_{Sh} parallel resistance, R_S serial resistance, C_d parallel capacitance, R_L working resistance, (b) schematic of the photodiode in the PC mode: (1) the depletion region, (2) drifting region (3) electron and hole diffusion region. Adapted from [21].

The Equation (1.26) shows that the current is a linear function of photocurrent P_λ and wavelength λ. From this equation can also be derived the current spectral sensitivity R_J (Fig. 1.14). The dashed line in Figure 1.14 shows the theoretical curve according to (1.26). The continuous line shows the real photodiode, also with the long-wavelength cutoff λ_g.

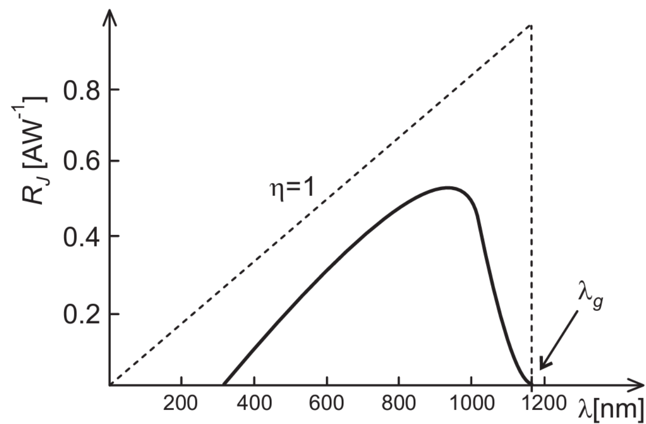

Figure 1.14: Spectral current sensitivity of photodiode dashed line showing the theoretical curve according to (1.26), continuous line showing the real photodiode, λ_g depicting the long-wavelength cutoff. Adapted from [21].

1.4 Wave Propagation in Layered Medium

A medium whose properties are constant in the x and y direction, dependent on one Cartesian coordinate only, is called a layered medium. The properties of layered media are usually expressed in terms of matrices. For the homogenous dielectric film the characteristic matrix $\mathbf{M}(z)$ for the Transverse Electric (TE) wave is seen to be [22]

$$\mathbf{M}(z) = \begin{bmatrix} \cos(k_0 nz\cos\theta) & -\frac{i}{p}\sin(k_0 nz\cos\theta) \\ -ip\sin(k_0 nz\cos\theta) & \cos(k_0 nz\cos\theta) \end{bmatrix}, \tag{1.27}$$

θ being the incidence angle, n the refractive index, z the height of the medium and $k_0 = \frac{2\pi}{\lambda_0}$. p being set to

$$p = \sqrt{\frac{\epsilon}{\mu}}\cos\theta, \tag{1.28}$$

the matrix for Transverse Magnetic (TM) wave can be obtained by replacing p by q

$$q = \sqrt{\frac{\mu}{\epsilon}}\cos\theta, \tag{1.29}$$

Reflection and Transmission Coefficients

Consider a layered medium extended from $z = 0$ to $z = z_1$ and bounded by two semi-infinite mediums, where a plane wave is incident upon it. The amplitudes of the electric vectors for the incident, transmitted, and reflected waves are denoted as A, T, and R respectively. The dielectric constants and magnetic permeabilities of the first and last medium are represented as ϵ_1, μ_1, ϵ_l, and μ_l. The angles θ_1 and θ_l are formed by the normals of the incident and transmitted waves with respect to the z-direction.

For the TE wave, the following relations hold true [22]

$$\left.\begin{aligned} U_0 &= A + R, \quad & U(z_1) &= T, \\ V_0 &= p_1(A - R), \quad & V(z_1) &= p_l T, \end{aligned}\right\} \tag{1.30}$$

where

$$p_1 = \sqrt{\frac{e_1}{\mu_1}}\cos\theta_1, \qquad p_l = \sqrt{\frac{e_l}{\mu_l}}\cos\theta_l. \tag{1.31}$$

The four quantities U_0, V_0, U and V given by (1.30) are connected by the realations [22]

$$\left.\begin{aligned} A + R &= (m'_{11} + m'_{12}p_l)T, \\ p_1(A - R) &= (m'_{21} + m'_{22}p_l)T. \end{aligned}\right\} \tag{1.32}$$

m'_{ij}, the elements of the characteristic matrix of the medium, evaluated for $z = z_1$.

From (1.32) the transmission and reflection coefficients of the film can be obtained

$$r = \frac{R}{A} = \frac{(m'_{11} + m'_{12}p_l)p_1 - (m'_{21} + m'_{22}p_l)}{(m'_{11} + m'_{12}p_l)p_1 + (m'_{21} + m'_{22}p_l)}, \tag{1.33}$$

$$t = \frac{T}{A} = \frac{2p_1}{(m'_{11} + m'_{12}p_l)p_1 + (m'_{21} + m'_{22}p_l)}. \tag{1.34}$$

The *reflectivity* and *transmissivity* in the terms of r and t are

$$\mathcal{R} = |r|^2 \qquad \mathcal{T} = \frac{p_l}{p_1}|t|^2. \tag{1.35}$$

Corresponding expressions for the TM wave can be derived by replacing p_1 and p_t in (1.33-1.35) by

$$q_1 = \sqrt{\frac{\mu_1}{\epsilon_1}}\cos\theta_1, \qquad q_l = \sqrt{\frac{\mu_t}{\epsilon_t}}\cos\theta_t. \tag{1.36}$$

A Dielectric Film Between Two Dielectric Media

Now the expressions for the dielectric film between two dielectric media can be derived. In Figure 1.15 is shown the basic structure of the problem. It is assumed that the media is non-magnetic ($\mu = 1$).

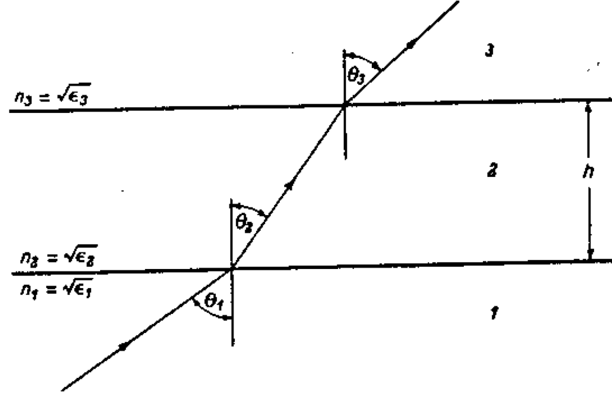

Figure 1.15: Propagation of an electromagnetic wave through a homogenous dielectric film, consisting of three dielectric media labeled 1,2,3, with corresponding refraction indexes n_j. θ_j marking the incident and transmitted angles, h the height of the second medium ($j = 1, 2, 3$). Adapted from [22].

The characteristic matrix of the problem is given by (1.27). Quantities referring to the three media (see Fig. 1.15) are denoted by subscripts 1,2 and 3

$$m'_{11} = m'_{22} = \cos\beta, \quad m'_{12} = -\frac{i}{p_2}\sin\beta, \quad m'_{21} = -ip_2\sin\beta, \tag{1.37}$$

where β is equal to

$$\beta = \frac{2\pi}{\lambda_0} n_2 h \cos\theta_2, \tag{1.38}$$

and

$$p_j = n_j \cos\theta_j \qquad (j = 1, 2, 3). \tag{1.39}$$

By substituting (1.37) into (1.33) and (1.34) the reflection and transmission coefficients r and t may be obtained, with $l = 3$. The resulting expressions can be expressed correspondingly to the first and second interface by r_{12}, t_{12} and r_{23}, t_{23}. For the TE, 12 interface we get

$$r_{12} = \frac{n_1 \cos\theta_1 - n_2 \cos\theta_2}{n_1 \cos\theta_1 + n_2 \cos\theta_2} \tag{1.40}$$

$$t_{12} = \frac{2n_1 \cos\theta_1}{n_1 \cos\theta_1 + n_2 \cos\theta_2}, \tag{1.41}$$

With analogical expressions for the 23 interface, the refraction and reflection coefficients can be derived

$$r = \frac{r_{12} + r_{23} e^{2i\beta}}{1 + r_{12} r_{23} e^{2i\beta}} \tag{1.42}$$

$$t = \frac{t_{12} t_{23} e^{i\beta}}{1 + r_{12} r_{23}}, \tag{1.43}$$

then from equations (1.42) and (1.43) can the reflectivity and transivity be derived

$$\mathcal{R} = |r|^2 = \frac{r_{12}^2 + r_{23}^2 + 2r_{12}r_{23}\cos 2\beta}{1 + r_{12}^2 r_{23}^2 + 2r_{12}r_{23}\cos 2\beta}, \tag{1.44}$$

$$\mathcal{T} = \frac{n_3 \cos\theta_3}{n_1 \cos\theta_1} |t|^2 = \frac{n_3 \cos\theta_3}{n_1 \cos\theta_1} \frac{t_{12}^2 t_{23}^2}{1 + r_{12}^2 r_{23}^2 + 2r_{12}r_{23}\cos 2\beta}, \tag{1.45}$$

An Absorbing Film on a Transparent Substrate

Similarly to the dielectric film, the optical properties are dependent on one Cartesian coordinate only (z). However, because of the addition of conducting medium to the dielectric constant ε and magnetic permeability μ, there may be a finite conductivity σ, which is also a function of this one coordinate alone.

The equations for the propagation of the layered media in dielectric media remain valid provided that the real dielectric constant ε and the real wavenumber k are replaced by the complex dielectric constant $\hat{\varepsilon} = \varepsilon + \frac{i4\pi\sigma}{\omega}$ and by the complex wave number $\hat{k} = \frac{\omega\sqrt{\mu(\varepsilon + \frac{i4\pi\sigma}{\omega})}}{c}$. Hence the absorbing stratified medium can be characterized by a two-by-two matrix also containing complex numbers in contrast to stratified dielectric medium with elements of pure imaginary or real numbers.

Considering a plane-parallel conducting film between two dielectric media (Fig. 1.16). The formulae relating to the reflection and transition of a plane monochromatic wave by the film can be modified by replacing the refractive index n_2 by $\hat{n}_2 = n_2(1 + i\kappa_2)$. It is convenient to set $\hat{n}_2 \cos\theta_2$ to

$$\hat{n}_2 \cos\theta_2 = u_2 + iv_2, \tag{1.46}$$

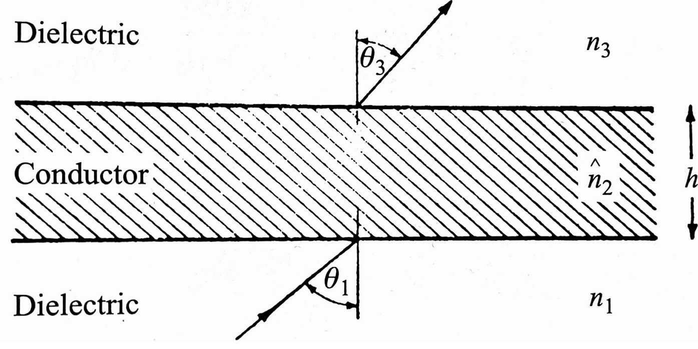

Figure 1.16: An absorbing film situated between two dielectric media, divided into three parts labeled 1,2,3. 1 and 3 being dielectric, while 2 being a conductor with corresponding refraction indexes n_1, n_3 and $\hat{n}_2$ (hat indicating absorbing medium), θ_j marking the incident and transmitted angles, h the height of the second medium ($j = 1, 2, 3$). Adapted from [22].

where u_2 and v_2 are real. u_2 and v_2 can easily be expressed in terms of the angle of incidence and the characterizing optical constants of the first and second medium by squaring (1.46) and using Snell‘s law $\hat{n}_2 \sin\theta_2 = n_1 \sin\theta_1$, that

$$(u_2 + iv_2)^2 = \hat{n}_2^2 - n_1^2 \sin^2\theta_1. \tag{1.47}$$

Equating the real and imaginary parts

$$\left.\begin{aligned} u_2^2 - v_2^2 &= n_2^2(1-\kappa_2^2) - n_1^2 \sin^2\theta_1, \\ u_2 v_2 &= n_2^2 \kappa_2. \end{aligned}\right\} \tag{1.48}$$

From (1.48) can be derived

$$\left.\begin{aligned} 2u_2^2 &= n_2^2(1-\kappa_2^2) - n_1^2 \sin^2\theta_1 + \sqrt{[n_2^2(1-\kappa_2^2) - n_1^2 \sin^2\theta_1]^2 + 4n_2^4\kappa_2^2}, \\ 2v_2^2 &= -[n_2^2(1-\kappa_2^2) - n_1^2 \sin^2\theta_1] + \sqrt{[n_2^2(1-\kappa_2^2) - n_1^2 \sin^2\theta_1]^2 + 4n_2^4\kappa_2^2}. \end{aligned}\right\} \tag{1.49}$$

Next, the reflection r and transition t coefficients for interfaces 1-2 and 2-3 are evaluated. For the sake of simplicity, the perpendicular and parallel electric vectors are considered separately.

Electric vector perpendicular to the plane of incidence (TE wave). For this instance, replacing $n_2 \cos\theta_2$ by $\hat{n}_2 \cos\theta_2 = u_2 + iv_2$ in (1.40) and (1.41) the equations become

$$r_{12} = \rho_{12} e^{i\phi_{12}} = \frac{n_1 \cos\theta_1 - (u_2 + iv_2)}{n_1 \cos\theta_1 + (u_2 + iv_2)}. \tag{1.50}$$

From (1.50) can be derived

$$\rho_{12}^2 = \frac{(n_1 \cos\theta_1 - u_2)^2 + v_2^2}{(n_1 \cos\theta_1 + u_2)^2 + v_2^2}, \quad \tan\phi_{12} = \frac{2v_2 n_1 \cos\theta_1}{u_2^2 + v_2^2 - n_1^2 \cos^2\theta_1}. \tag{1.51}$$

For transmission at the first interface, we have

$$t_{12} = \tau_{12} e^{i\chi_{12}} = \frac{2n_1 \cos\theta_1}{n_1 \cos\theta_1 + u_2 + iv_2}. \tag{1.52}$$

which gives

$$\tau_{12}^2 = \frac{(n_1 \cos\theta_1)^2}{(n_1 \cos\theta_1 + u_2)^2 + v_2^2}, \quad \tan\chi_{12} = \frac{v_2}{n_1 \cos\theta_1 + u_2}. \tag{1.53}$$

Analogically the equations for transmission and reflection can be obtained on the second interface

$$\rho_{23}^2 = \frac{(n_3 \cos\theta_3 - u_2)^2 + v_2^2}{(n_3 \cos\theta_3 + u_2)^2 + v_2^2}, \quad \tan\phi_{23} = \frac{2v_2 n_3 \cos\theta_3}{u_2^2 + v_2^2 - n_3^2 \cos^2\theta_3}. \tag{1.54}$$

$$\tau_{23}^2 = \frac{4(u_2^2 + v_2^2)}{(n_3 \cos\theta_3 + u_2)^2 + v_2^2}, \quad \tan\chi_{23} = \frac{v_2 n_3 \cos\theta_3}{u_2^2 + v_2^2 + u_2 n_3 \cos\theta_3}. \tag{1.55}$$

Electric vector parallel to the plane of incidence (TM wave). The equations for the TM wave can be obtained from those for the TE wave by substituting the $p_j = \cos\theta_j$ by $q_j = \frac{\cos\theta_j}{n_j}$, assuming that the media are nonmagnetic. The reflection and transition coefficients r, t now refer to the ratios of the TM vectors

$$\begin{aligned} r_{12} = \rho_{12} e^{i\phi_{12}} &= \frac{\frac{1}{n_1}\cos\theta_1 - \frac{1}{\hat{n}_2}\cos\theta_2}{\frac{1}{n_1}\cos\theta_1 + \frac{1}{\hat{n}_2}\cos\theta_2} = \frac{\hat{n}_2^2 \cos\theta_1 - n_1 \hat{n}_2 \cos\theta_2}{\hat{n}_2^2 \cos\theta_1 + n_1 \hat{n}_2 \cos\theta_2} \\ &= \frac{[n_2^2(1-\kappa_2^2) + 2in_2^2\kappa_2]\cos\theta_1 - n_1(u_2 + iv_2)}{[n_2^2(1-\kappa_2^2) + 2in_2^2\kappa_2]\cos\theta_1 + n_1(u_2 + iv_2)}. \end{aligned} \tag{1.56}$$

From (1.56) we get

$$\left.\begin{aligned} \rho_{12}^2 &= \frac{[n_2^2(1-\kappa_2^2)\cos\theta_1 - n_1 u_2]^2 + [2n_2^2\kappa_2\cos\theta_1 - n_1 v_2]^2}{[n_2^2(1-\kappa_2^2)\cos\theta_1 + n_1 u_2]^2 + [2n_2^2\kappa_2\cos\theta_1 + n_1 v_2]^2}, \\ \tan\phi_{12} &= 2n_1 n_2^2 \cos\theta_1 \frac{2\kappa_2 u_2 - (1-\kappa_2^2)v_2}{n_2^4(1+\kappa_2^2)^2\cos^2\theta_1 - n_1^2(u_2^2 + v_2^2)}. \end{aligned}\right\} \tag{1.57}$$

For the transition coefficient after replacing $n_j \cos\theta_j$ by $\frac{\cos\theta_j}{n_j}$

$$\begin{aligned} t_{12} = \tau_{12} e^{i\chi_{12}} &= \frac{\frac{2}{n_1}\cos\theta_1}{\frac{1}{n_1}\cos\theta_1 + \frac{1}{\hat{n}_2}\cos\theta_2} \\ &= \frac{2[n_2^2(1-\kappa_2^2) + 2in_2^2\kappa_2]\cos\theta_1}{[n_2^2(1-\kappa_2^2) + 2in_2^2\kappa_2]\cos\theta_1 + n_1(u_2 + iv_2)}. \end{aligned} \tag{1.58}$$

From (1.58) we get

$$\left.\begin{aligned} \tau_{12}^2 &= \frac{4n_2^4(1+\kappa_2^2)^2\cos^2\theta_1}{[n_2^2(1-\kappa_2^2)\cos\theta_1 + n_1 u_2]^2 + [2n_2^2\kappa_2\cos\theta_1 + n_1 v_2]^2}, \\ \tan\chi_{12} &= \frac{n_1[2\kappa_2 u_2 - (1-\kappa_2^2)v_2]}{n_2^2(1+\kappa_2^2)^2\cos\theta_1 + n_1[(1-\kappa_2^2)u_2 + 2\kappa_2 v_2]}. \end{aligned}\right\} \tag{1.59}$$

Similarly, we get the coefficients for transition and reflection for the second interface

$$\left.\begin{aligned}\rho_{23}^2 &= \frac{[n_2^2(1-\kappa_2^2)\cos\theta_3 - n_3u_2]^2 + [2n_2^2\kappa_2\cos\theta_3 - n_3v_2]^2}{[n_2^2(1-\kappa_2^2)\cos\theta_3 + n_3u_2]^2 + [2n_2^2\kappa_2\cos\theta_3 + n_3v_2]^2},\\ \tan\phi_{23} &= 2n_3n_2^2\cos\theta_3\frac{2\kappa_2u_2 - (1-\kappa_2^2)v_2}{n_2^4(1+\kappa_2^2)^2\cos^2\theta_3 - n_3^2(u_2^2+v_2^2)}.\end{aligned}\right\} \tag{1.60}$$

and

$$\left.\begin{aligned}\tau_{23}^2 &= \frac{4n_3^2(u_2^2+v_2^2)}{[n_3u_2 + n_2^2(1-\kappa_2^2)\cos\theta_3]^2 + (n_3v_2 + 2n_2^2\kappa_2\cos\theta_3)^2},\\ \tan\chi_{23} &= \frac{n_2^2[1-\kappa_2)^2v_2 - 2\kappa_2u_2]\cos\theta_3}{n_3(u_2^2+v_2^2) + n_2^2[(1-\kappa_2)^2u_2 + 2\kappa_2v_2]\cos\theta_3}.\end{aligned}\right\} \tag{1.61}$$

Knowing the equations for the ρ_{12}, ϕ_{12}, etc. we can obtain the complex reflection $\mathcal{R}$ and transmission $\mathcal{T}$ coefficients of the film. It is useful to set η to

$$\eta = \frac{2\pi}{\lambda_0}h, \tag{1.62}$$

where h is the thickness of the second layer and λ_0 is the wavelength of the light. Than β equals

$$\beta = \frac{2\pi}{\lambda_0}\hat{n}_2h\cos\theta_2 = (u_2 + iv_2)\eta. \tag{1.63}$$

Now put together equations (1.58-1.61) become

$$r = \rho e^{i\delta_r} = \frac{\rho_{12}e^{i\phi_{12}} + \rho_{23}e^{-2v_2\eta}e^{i(\phi_{23}+2u_2\eta)}}{1 + \rho_{12}\rho_{23}e^{-v_2\eta}e^{i(\phi_{12}+\phi_{23}+2u_2\eta)}}, \tag{1.64}$$

$$rt = \tau e^{i\delta_t} = \frac{\tau_{12}\tau_{23}e^{-2v_2\eta}e^{i(\chi_{12}+\chi_{23}+u_2\eta)}}{1 + \rho_{12}\rho_{23}e^{-v_2\eta}e^{i(\phi_{12}+\phi_{23}+2u_2\eta)}}, \tag{1.65}$$

From (1.64) can be derived the following expression for the reflectivity $\mathcal{R}$ and for the phase change δ_r on reflection

$$\mathcal{R} = |r|^2 = \frac{\rho_{12}^2e^{2v_2\eta} + \rho_{23}^2e^{-2v_2\eta} + 2\rho_{12}\rho_{23}\cos(\phi_{23} - \phi_{12} + 2u_2\eta)}{e^{2v_2\eta} + \rho_{12}^2\rho_{23}^2e^{-2v_2\eta} + 2\rho_{12}\rho_{23}\cos(\phi_{12} + \phi_{23} + 2u_2\eta)}, \tag{1.66}$$

$$\tan\delta_r = \frac{\rho_{23}(1-\rho_{12}^2)\sin(2u_2\eta + \phi_{23}) + \rho_{12}(e^{2v_2\eta} - \rho_{23}^2e^{-2v_2\eta})\sin\phi_{12}}{\rho_{23}(1+\rho_{12}^2)\cos(2u_2\eta + \phi_{23}) + \rho_{12}(e^{2v_2\eta} - \rho_{23}^2e^{-2v_2\eta})\cos\phi_{12}}. \tag{1.67}$$

Both of these equations are valid for TE and TM waves.

Similarly, we can obtain equations for the transmissivity $\mathcal{T}$ and for the phase change δ_t on

$$\begin{aligned}\mathcal{T} &= \frac{n_3\cos\theta_3}{n_1\cos\theta_1}|t|^2\\ &= \frac{n_3\cos\theta_3}{n_1\cos\theta_1}\frac{\tau_{12}^2\tau_{23}^2e^{-2v_2\eta}}{1 + \rho_{12}^2\rho_{23}^2e^{-4v_2\eta} + 2\rho_{12}\rho_{23}e^{-2v_2\eta}\cos(\phi_{12} + \phi_{23} + 2u_2\eta)},\end{aligned} \tag{1.68}$$

$$\tan[\delta_t - \chi_{12} - \chi_{23} + u_2\eta] = \frac{e^{2v_2\eta}\sin 2u_2\eta - \rho_{12}\rho_{23}\sin(\phi_{12}+\phi_{23})}{e^{2v_2\eta}\cos 2u_2\eta + \rho_{12}\rho_{23}\cos(\phi_{12}+\phi_{23})}. \quad (1.69)$$

For TM wave the factor $\frac{n_3\cos\theta_3}{n_1\cos\theta_1}$ must be replaced by $\frac{n_1\cos\theta_3}{n_3\cos\theta_1}$. Figure 1.17 showcases several typical cases, where the dependence of reflectivity and transmissivity on the film's thickness is illustrated, both with and without absorption κ_2.

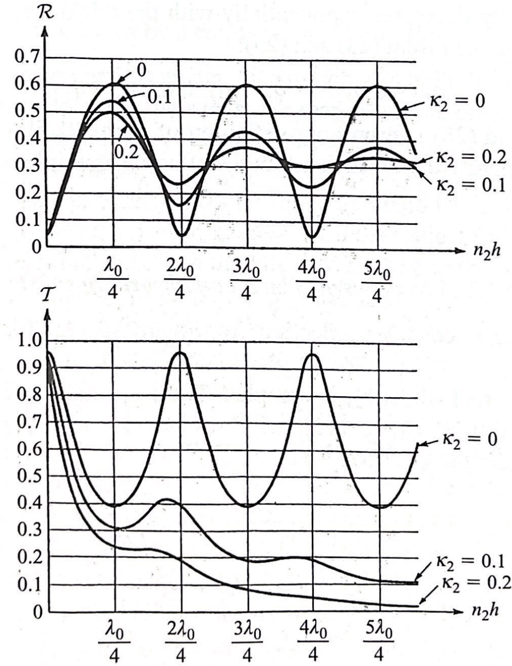

Figure 1.17: The reflectivity $\mathcal{R}$ and transmissivity $\mathcal{T}$ of a metallic film as functions of its optical thickness for normal incidence. $[n_1 = 1; n_2 = 3,5; n_3 = 1,5; \kappa_1 = \kappa_3 = 0; \theta_1 = 0]$ Adapted from [22].

2. Construction of Optical Scanning Profilometer

This chapter will deal with motivation, technical details, and the construction process of our automated experimental setup. Our goals were:

1. Construct a machine capable of measuring the uniformity of layer deposited by the MBE. It should utilize both transmission and reflection of samples on translucent substrates, as well as reflection for samples on opaque substrates.
2. Optimize the design for maximum material efficiency and compactness.
3. Do so without being too complex or expensive. Thus we used 3D printing and commercially available parts.

2.1 Construction of Experimental Setup

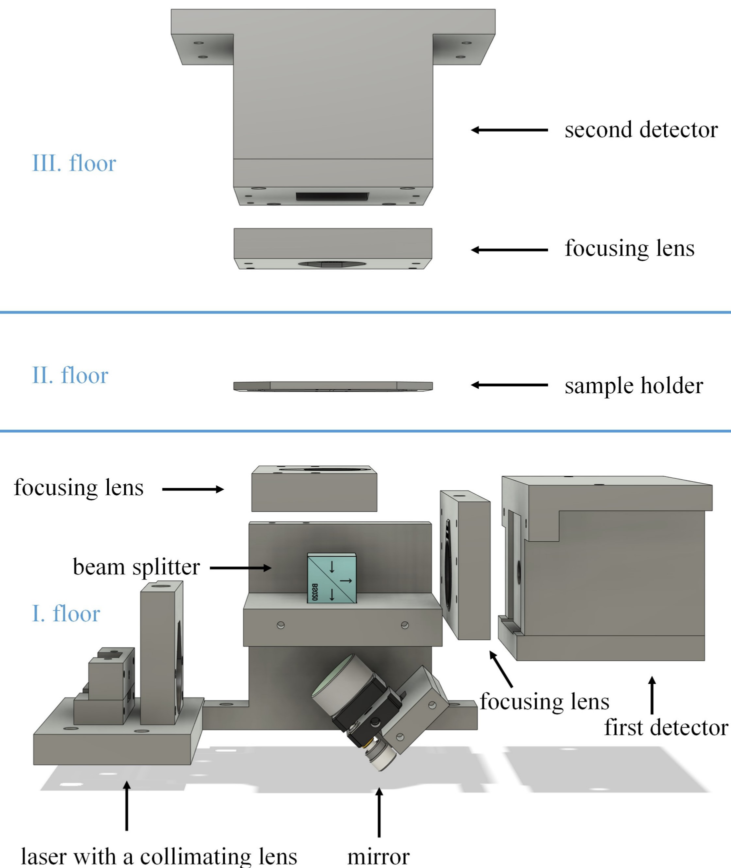

Figure 2.1: The setup without the aluminum skeleton and core-xy movement system.

Firstly, we drew a rough sketch of our desired setup and decided what materials to use. We opted to use an aluminum profile with dimensions of 20x20 mm for

the main structure for its lightness and low cost. We divided this structure into three parts, each representing one floor of the setup. With the sketch finished, we modeled the design in Fusion 360. The 3-floor setup without the motion system and the aluminum skeleton is shown in Figure 2.1.

2.1.1 First Floor

On the first floor of our setup is a laser diode, one detector, a collimating aspherical lens, two focusing lenses, one in front of the detector and one in front of the sample, a mirror, and a beam-splitter, with an arrangement that collimates the laser diode's output, which is then passed through the beam splitter and focused on the sample. The beam splitter redirects the reflected beam from the sample to the photodiode with its own focusing lens. We chose the laser diode with a wavelength of 658 nm (Thorlabs L658P040) in order to be able to perform transmission measurements of various substrates, including GaP and Sapphire, with bandgaps of 550 nm and 120 nm, respectively. For the photodiodes, we selected the Si photodiode FDS010 from Thorlabs, with a detection range of 200-1100 nm and a peak response at the wavelength of around 730 nm. The selection of this particular photodiode was based on its favorable cost-to-performance ratio. Our laser diode has a beam divergence provided by the manufacturer of 10 and 20 degrees for the ZZ and YY axis respectively, so we chose the ACL25416U-A collimation lens from Thorlabs, with an Anti-Reflective Coating (ARC) of 350-700 nm and a short back focal length of 7,3 mm to achieve a collimated beam width of approximately 1 cm. All the other lenses in our setup were selected based on their compatibility with our setup and budget. They all have ARC for the range of 350-700 nm. The beam splitter we used is the BS079 by Thorlabs, with a 30:70 (reflection:transmission) split ratio and ARC for the 350-700 nm range.

2.1.2 Second Floor

The second floor consists of the mechanical motion system and the sample holder. Since we needed to have the central region unobstructed to allow propagation of the laser beam, we chose the core-xy Cartesian motion system (shown in Fig.2.2). We modeled the core-xy system according to Fig. 2.2, putting the components 9,7 and 8,10 on each other to save space. Some parts were manufactured from aluminum to increase their stiffness and prevent bending (grey parts in Figure 2.3) for better resistance to bending. These parts were cut out to size by a Computer Numerical Control (CNC) machine. The belt, motors, and bearing holders (orange in Fig. 2.3) were 3d printed. These aluminum plates and holders were placed on the HIWIN MGN series 7 linear guideways. For the stepper motors, we choose the nema 11 motors for their compact size and low weight. These were connected to the Bigtreetech SKR V1.3 control board for 3d printers, with firmware which adapted for our purposes. The stepper motor drivers we used were the TMC2209 V1.2 by Bigtreetech.

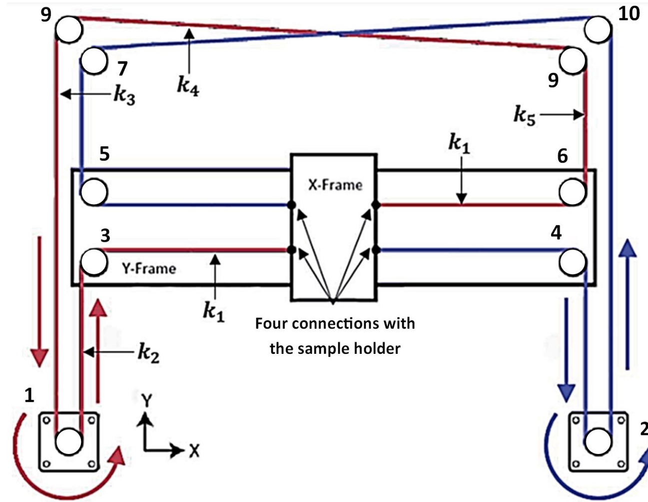

Figure 2.2: Schematics of Core-XY system, two belts (in red and blue) connected with the ample holder at four points symmetrically. Components 1 and 2 are the stationary driving units at four points symmetrically. Components 3-10 are the idle pulleys. Adapted from [23].

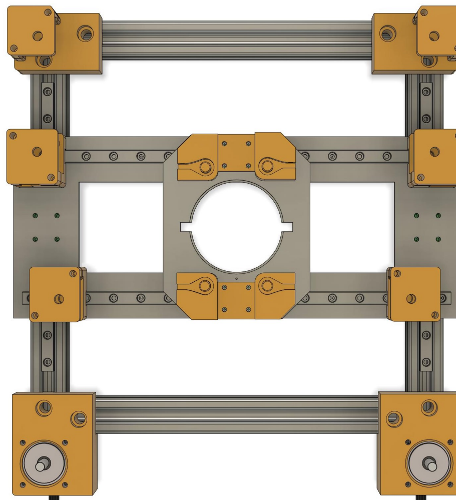

Figure 2.3: 3d model of the core-xy system.

2.1.3 Third Floor

The third floor is the simplest, containing just one detector for measuring the transmitted light, having the same photodiode FDS010 from Thorlabs as the first one and a bi-convex focusing lens, with ARC for the range of 350-700 nm, positioned between the sample and the detector.

2.2 Measuring Process

The measurement of our samples requires synchronizing two aspects: the movement of the sample and the measurement of transmitted or reflected light. This chapter focuses on the realization of the measurement of a circular sample and

programming a custom script to synchronize the movement of the sample with the measurement of transmitted or reflected light.

2.2.1 Programming of the Measurement

Measurement is controlled via the computer, which communicates with all of the connected devices. The measurement routine is programmed in Python due to the ease of use and wide data processing capabilities of the accompanied Python libraries. Since our samples have a circular shape with a 2-inch diameter, and our mechanical motion system is most precise in single-axis movement, we developed a procedure of dividing the circle into squares. Each square is positioned such that its center lies within the circular boundary of the sample. Consequently, we can assign measurement positions to each square center. This approach enables us to accelerate the data collection process by performing measurements in a linear, line-by-line manner instead of circular trajectories, eliminating the need for two movements per measurement point. Figure 2.4 shows the division of the sample into measurement positions, with each position spaced 0,5 mm apart. For more precise measurements, we can go as low as 10 μm with the step, allowing us to match the steep with the spot size of the laser.

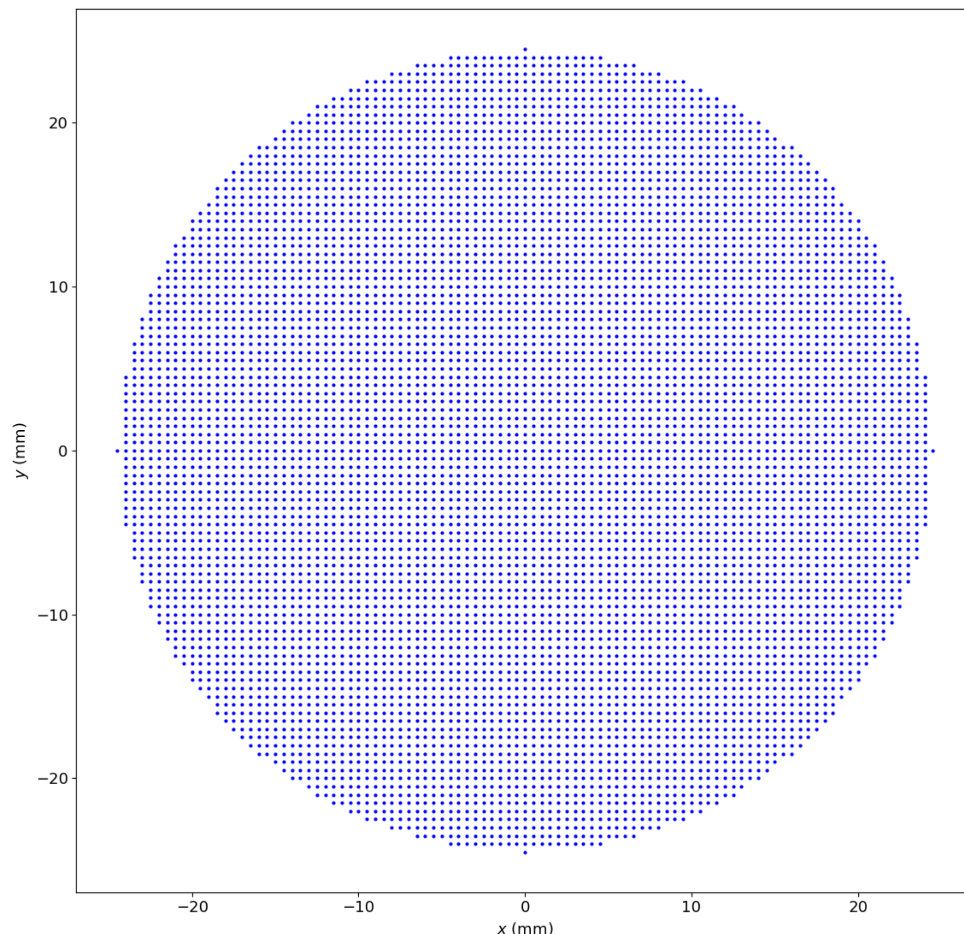

Figure 2.4: 2-inch sample divided into 0,5 mm long squares, the blue dots show the centers of the squares.

To achieve the required level of precision, we reprogrammed the Marlin firmware of the board. Although primarily designed for 3D printers that typically don't require such fine movements, we made adjustments to the firmware parameters to accommodate our needs. With this modification, we were able to fully utilize our setup. We communicate with the devices via USB, sending them commands. The control board follows commands in G-code, a CNC programming language used mainly by machine tools as well as 3d printers. The voltmeters connected to the photodiodes follow their specific device commands. The measurement sequence is the following. We send the coordinates to the control board, which moves the sample to the desired place, then wait until the movement is executed. After that, we take the measurement from the voltmeter averaging 10 points with an acquisition window of 20 ms resulting in 200 ms needed for each point. We have the flexibility to adjust the number of averaging points according to our specific requirements. This allows us to choose between faster measurements with less precision by reducing the averaging points or slower measurements with higher precision by increasing the averaging points. Then we save the measured values with their position into a data file, which we can later process. This procedure then repeats until all the positions are measured.

2.2.2 Measurement Devices

To measure the transmission and reflection of the samples, we used amplified detectors utilizing photodiodes mentioned in chapter 1.3 with their amplification circuits manufactured by Miroslav Dušek from the Department of chemical physics and optics.

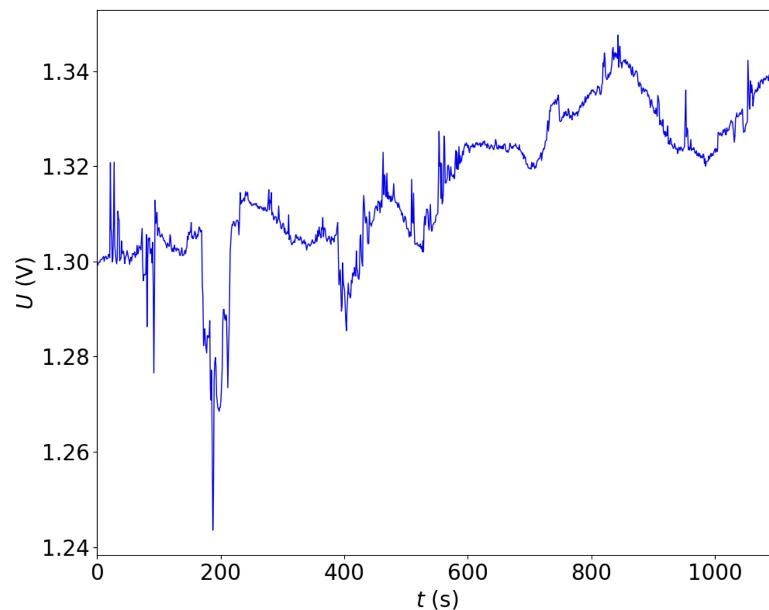

Figure 2.5: The measurement of long-term continuous laser stability with detectors directly connected to the voltmeter.

At first, we measured the voltage from the detectors directly by Keithley DMM6500. However, because of the broadband sensitivity of our photodiode, the measurement was contaminated by the light noise of the surrounding light.

In Figure 2.5 can be seen the instability of the signal is caused by the changes in the lighting in the room.

In order to minimize the noise, we switched the power supply for the laser diode to a function generator and changed from continuous mode to pulsing mode. We added a lock-in amplifier, SR830 DSP by Stanford Research Systems, between our photodiode and voltmeter. A lock-in works by selectively amplifying a signal at a specific (reference) frequency while suppressing all other frequencies. Because lamps flicker at a frequency of 50 Hz, we chose a significantly higher frequency to avoid measuring this noise. As shown in Fig. 2.6, the noise is reduced significantly.

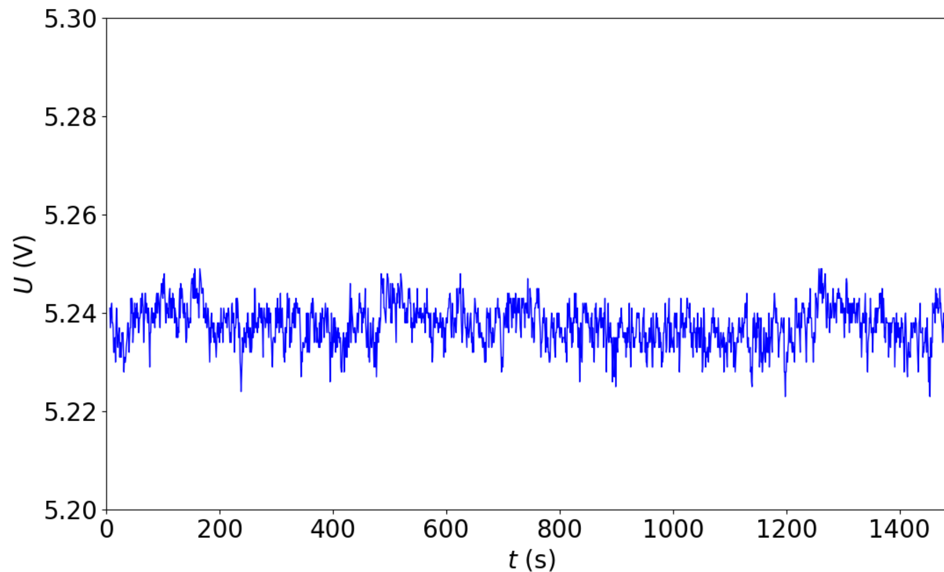

Figure 2.6: The measurement of long-term continuous laser stability with a lock-in amplifier added between the detector and voltmeter.

2.2.3 Spot size measurement

To find out the minimum possible step of our measurement, we used the knife-edge method to get the laser spot size in the sample's plane. For this, we used the edge of a razor blade positioned on a unique 3d printed holder, which replaced our sample holder. This holder was capable of holding the razor in two directions, x and y. Therefore, we were able to check the spot size in two perpendicular directions.

Knife-edge method

The knife-edge method is used to measure the parameters of a Gaussian laser beam. In this method, the intensity of light on the detector is directly related to the position of the knife edge. In Figure 2.7, when the knife edge moves along the x-direction, the intensity on the detector can be described by an equation [24]

$$
\begin{aligned}
I(x) &\approx \int_{-\infty}^{\infty}\int_{-\infty}^{x} e^{-2\frac{x'^2+y'^2}{w^2}}dx'dy' = \int_{-\infty}^{\infty} e^{-2\frac{y'^2}{w^2}}dy' \int_{-\infty}^{x} e^{-2\frac{x'^2}{w^2}}dx' \\
&= \frac{\pi w^2}{4}\left(1+erf\left(\frac{\sqrt{2}x}{w}\right)\right) = \frac{\pi w^2}{2}\left(1-\frac{1}{2}erfc\left(\frac{\sqrt{2}x}{w}\right)\right),
\end{aligned} \tag{2.1}
$$

where erf and $erfc$ are tabled functions, and w represents the diameter of the beam.

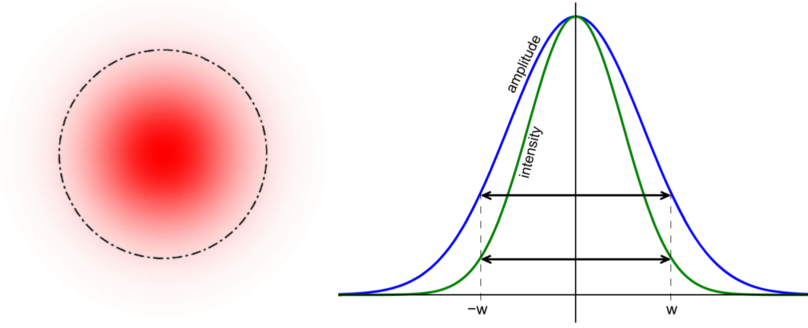

Figure 2.7: A typical pattern displaying the intensity of a laser beam (left) and the distributions of intensity and amplitude for a normalized Gaussian beam (right). Adapted from [25].

The measurements follow the intensity variation along one axis of the movement, which is then fitted using equation (2.1). The fitting process gives the parameter w as the output. An example showcasing the fitted data can be seen in figure 2.9.

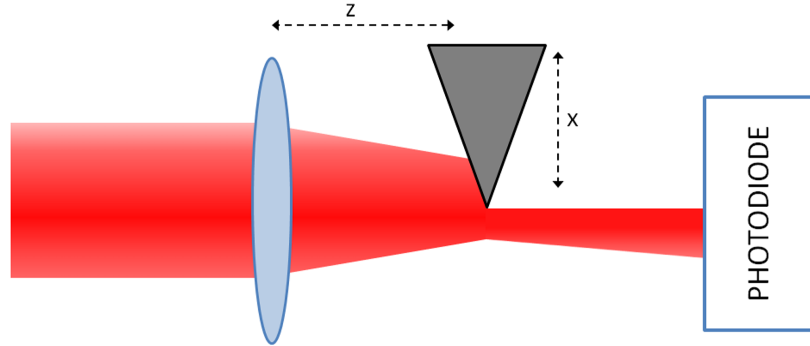

Figure 2.8: Schematic of a Knife Edge method. Adapted from [26].

The minimum spot size that we were able to achieve was 55 μm in x direction and 45 μm in the y direction. As can be seen in Figure 2.9, the laser spot's parameters were not optimal due to the spot not being completely symmetrical, which is understandable due to different divergence in the x and y axis from the laser diode itself. We intentionally did not compensate for this asymmetry to allow for the potential replacement of the laser diode with a different wavelength in the future. Although the fitting function does not initially correlate with the

graph, we can consider the fit of the measurement to be a reliable indicator of accuracy, as it aligns well with the first derivative of the measured data 2.10.

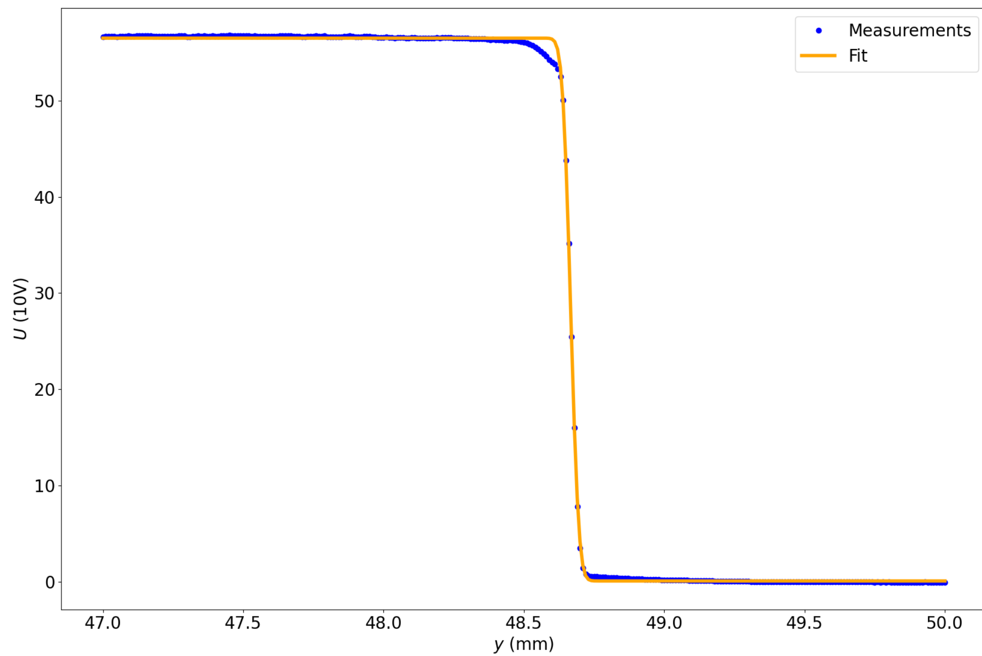

Figure 2.9: Example of the measured and fitted data using the knife-edge method in y direction.

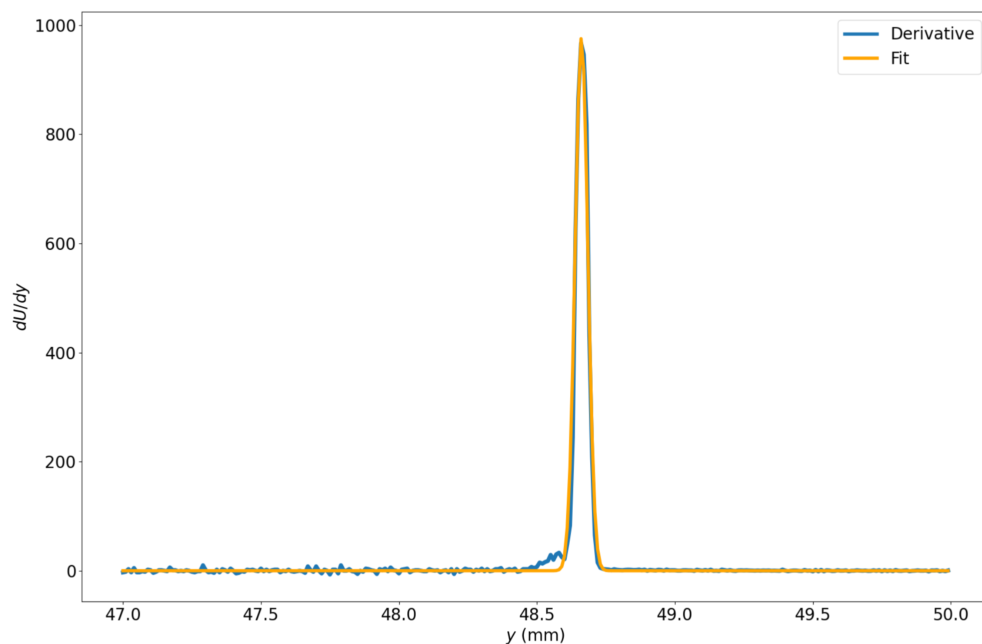

Figure 2.10: Comparison of the first derivative and fit of 2.9.

We designed our setup in a way that we were able to adjust the size of the spot by moving the lens at regular intervals from the knife edge, utilizing the interchangeability of the spacers holding the lens. Each 1mm movement of the lens resulted in a change in a spot size of approximately 30 μm. This feature

enables us to align the spot size with the measurement step size effectively, as we can 3D print the spacers reliably in height steps of 0,1 mm.

2.3 Data Analysis

The examination of our data involves addressing challenges related to identifying the uniform areas and dividing them into segments of the same uniformity, finding the highest and lowest signal points, and attempting to identify and eliminate any defects present in the film caused by factors other than deposition itself.

For the analysis of our measured data, we wrote a Python script that utilizes the Matplotlib library. This script was specifically designed to generate a 2D color map, allowing us to visualize the characteristics of the measured sample in a graphical format. The simple colormap can be seen in Figure 2.11.

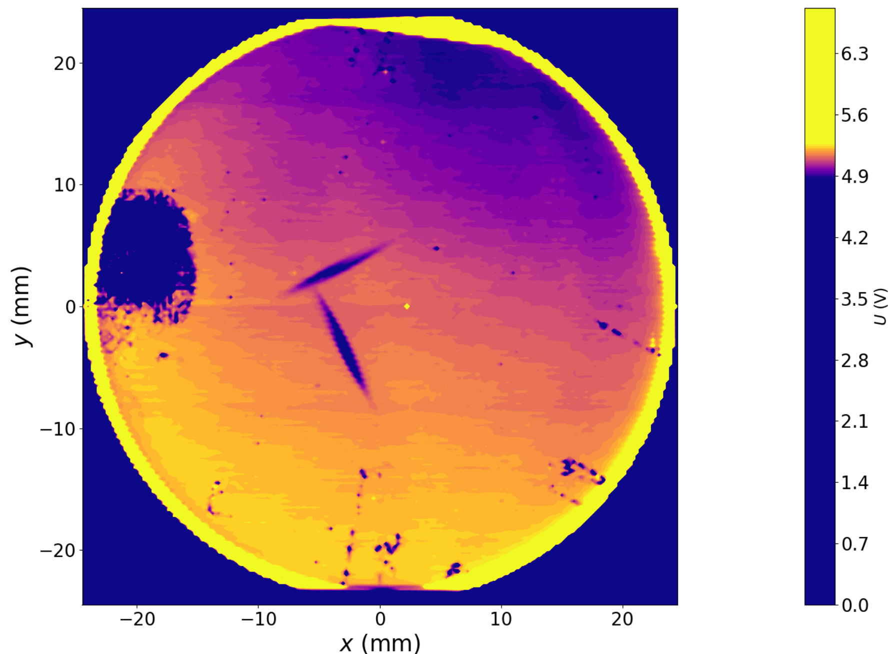

Figure 2.11: Basic colormap of the measured Gallium on Sapphire substrate.

In Figure 2.11, several dark dots and lines are visible, caused by sources other than the deposition itself, for example, dark lines caused by the incoming electron beam of the RHEED and unknown contamination on the left side, which was probably caused by improper handling that have an impact on the measurement. These irregularities disrupt the intensity of the passing laser beam, creating areas with no significance to our evaluation. We needed to identify these areas and remove them from the evaluation to limit their effect on the final results.

To eliminate these irregularities, we incorporated an additional component into our script. This component is designed to detect abrupt changes in the intensity of the laser beam and subsequently remove them from the data. By implementing this feature, we effectively mitigate most of the influence of these

disruptive elements on our analysis, resulting in cleaner and more reliable measurements.

By removing the irregularities, we gained improved accuracy in determining the maximum and minimum intensity values. Leveraging these values as reference points, we proceeded to scale the data from its minimum to maximum range. This scaling process allowed us to standardize the data and create equiuniform surfaces. Specifically, we divided the data into 20 surfaces, with each surface representing a distinct range of intensity. The division was structured so that there was a 5% change in intensity range between each consecutive surface. In order to visually distinguish and separate these surfaces, we incorporated contour lines into the visualization. In order to highlight the variations in intensity more effectively, we normalized the data by dividing it by the maximum intensity value. The improved colormap can be seen in Figure 2.12.

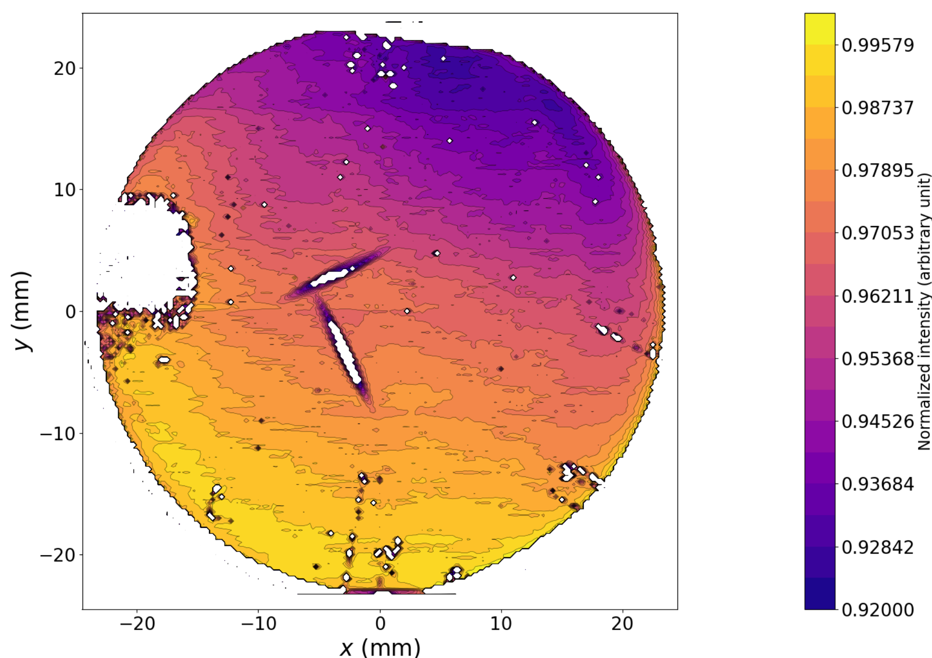

Figure 2.12: The improved colormap with removed irregularities and edge of the sample.

This method was used on all of our samples. Each figure presented in the subsequent chapter showcases the improved colormap

Once the irregularities were eliminated, we proceeded with the analysis by estimating the orientation of the effusion cells. We made the assumption that particle flow from the cell orifice exhibited axial symmetry. To ascertain the direction, we conducted the following steps: first, we located the central point of the sample and divided it into sections passing through this midpoint. Each section was then rotated by one degree relative to the previous one. Next, we identified the section displaying the most significant variation between the highest and lowest intensities. This particular section indicated the anticipated direction

of the effusion cell. The estimated direction was represented on the colormap using a black line 2.14.

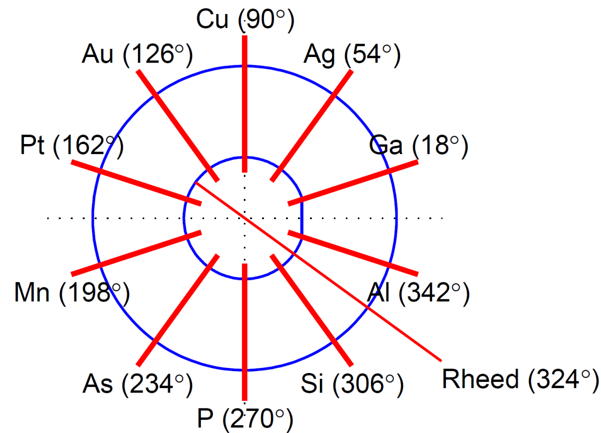

Figure 2.13: The internal geometry of effusion cells and RHEED in an MBE machine.

In order to assess the consistency between the estimated effusion direction and the actual geometry of the MBE machine, we initially established the rotation of the sample by referencing the fixed geometry of the RHEED line (visible line made by the electrons on the film) of 324° (Fig. 2.13) to the measured angle. Afterwards, we computed the updated angle of the effusion cell and represented it on the colormap using a dashed red line (Fig. 2.14).

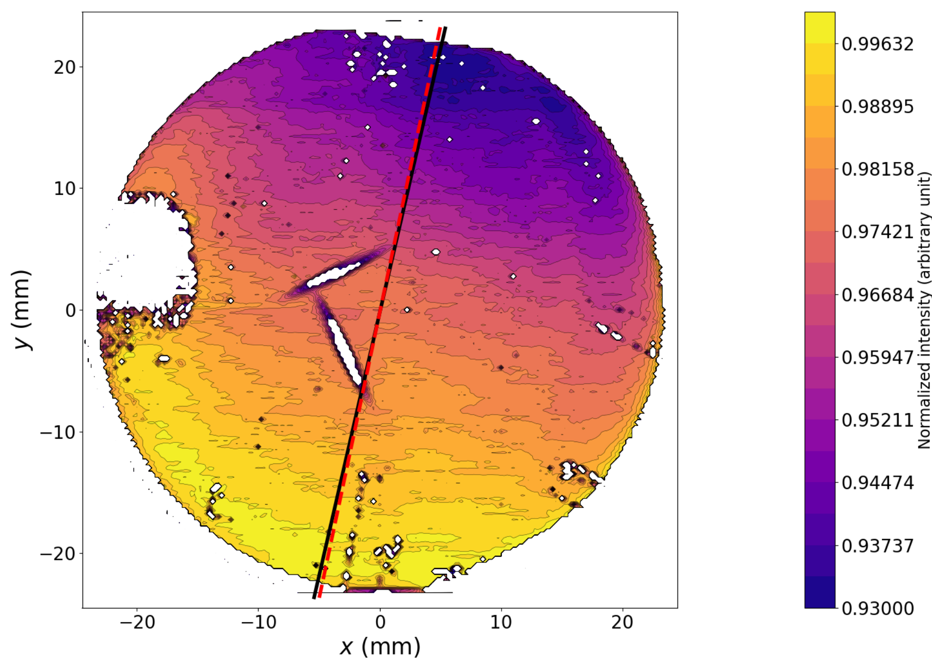

Figure 2.14: The improved colormap with a red dashed line depicting the real direction of the effusion cell and a black line, depicting the experimentally estimated direction.

2.3.1 Effects of Interference on Measurements

As illustrated in Figure 1.17 for the normal incidence of the laser beam, which corresponds with our device geometry, the reflectivity and transmissivity of the films exhibit a dependence on their thickness, characterized by damped oscillations. The initial minimum/maximum point on the graph corresponds to $\frac{\lambda_0}{4}$, where λ_0 represents the wavelength of our laser (658 nm) the quarter of which is approximately 165 nanometers. When comparing this value with the expected thickness range of our films, with a maximum thickness of 45 nanometers, we can confidently assert that the dependence of intensity in our measurements will be monotonous. Decreasing with thickness for transmissivity measurements and increasing for the reflectivity measurements. This fact will simplify the analysis of the films and eliminate the potential ambiguity of constructive and destructive interference separating the points of the highest thickness with the lowest intensity in transmissivity measurements and vice-versa.

3. Experimental Measurements

In this chapter, we present experimental measurements conducted for the thesis. As discussed in Chapter 1.4, the intensity of transmitted and reflected light through a conducting or dielectric layered medium is directly influenced by the thickness of the film.

We present the measurement of single-element films grown on translucent substrates. Each sample represents one effusion cell in our MBE machine. We analyze how light passes through and reflects depending on the uniformity of the molecular beam and discuss the findings in detail.

3.1 Sapphire Substrate

The uniformity of the conducting and dielectric film directly affects the intensity of transmitted and reflected light. Our measurement focused on this property with the goal of evaluating the changes in the thickness of the deposited film. This characteristic provides insights into the asymmetrical structure of the grown films, which can be attributed to the internal asymmetry or parameters of the effusion cell within the growth chamber of an MBE, which we discussed in Chapter 1.1.4.

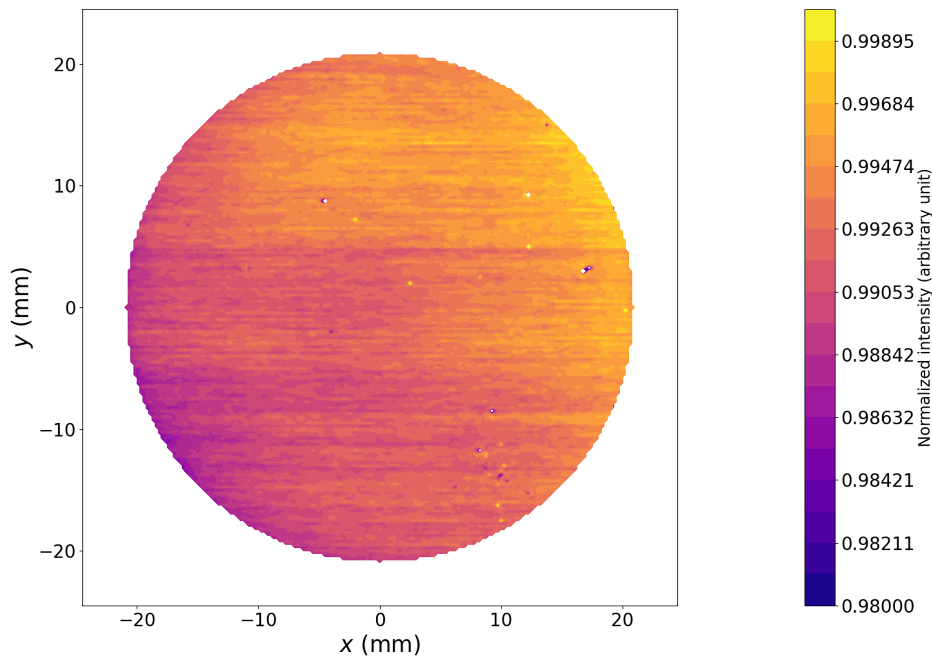

Figure 3.1: The transmission measurement of the clear substrate, the accuracy of the measurements and the effects of the lock-in noise are shown.

Figure 3.1 displays the transmission measurement of the sapphire substrate without any deposited film. The lighter and darker edges observed in the figure are attributed to the sample holder. It is worth noting that the overall variation in intensity across the substrate is less than 2% of the maximum, primarily influenced by the measurement noise as illustrated in Figure 2.6.

Films measured in this section were grown on the sapphire substrate. Sapphire substrate allows the widest set of measurements since it is transparent from the

wavelength of 120 nm. Even though different laser diode modules with different wavelengths are not currently utilized, these samples can be remeasured with different wavelengths in the future.

3.1.1 Copper

The first sample we measured was copper film grown on sapphire without any azimuthal rotation. By the estimate of the parameters of the effusion cell, the anticipated thickness of the film should be approximately 9,6 nanometers.

Figure 3.2 depicts a gradual change in uniformity, as indicated by the darker area on the left side transitioning to lighter edges of the sample. The abrupt change in color at the outer edge is a result of the transparent rim, where no film has been grown, leading to a sharp drop in absorption in that region. By comparing this result to the asymmetric geometry of the growth chamber, it can be assumed that the effusion cell was aiming from the left side of the sample holder. Consequently, more material was deposited on the left side of the substrate, leading to a gradual decrease in thickness from the maximum on the left side to the minimum on the right. The residue mark of the RHEED measurement during the film growth is clearly visible as a dark line in the middle. It is worth noting that in this particular sample, the RHEED line is thicker compared to the surrounding substrate, which may differ from the samples presented later on.

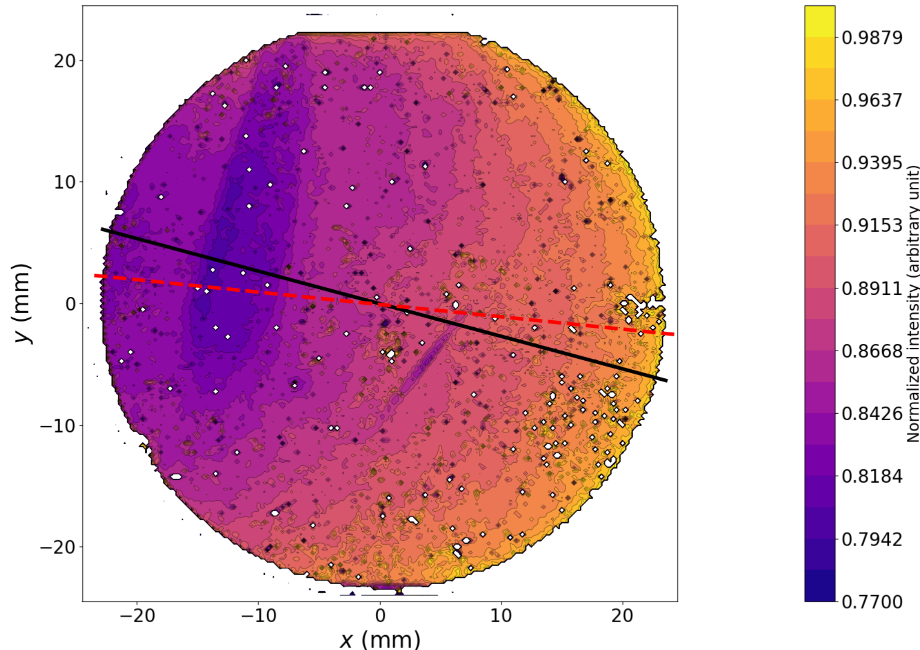

Figure 3.2: The transmission measurement of the copper sample, affected by the oxidation and dust particles, the uniformity change and RHEED line are clearly visible. The experimentally estimated direction of the effusion cell (black line) deviating from the real direction (red dashed line) by 9°.

The estimated direction of the effusion cell in the transmissivity measurements (indicated by the black line in Fig. 3.2) deviates by approximately 9° which is a bit less accurate than in the reflection measurement where the deviation was 8° (Fig. 3.3). This discrepancy can be attributed to the impact of oxidation, which tends to affect the transmitted intensity to a greater extent.

Figure 3.3 reveals that the reflection measurement exhibits an almost exact inverse pattern compared to the transmission measurement. This observation confirms the position of the effusion cell and the uniformity of the deposited film. The consistency in the patterns between these two measurements further supports our understanding of the sample's properties and enhances our confidence in drawing accurate conclusions, that the film on the left side is thicker than the right caused by the inclination of the effusion cell to this side.

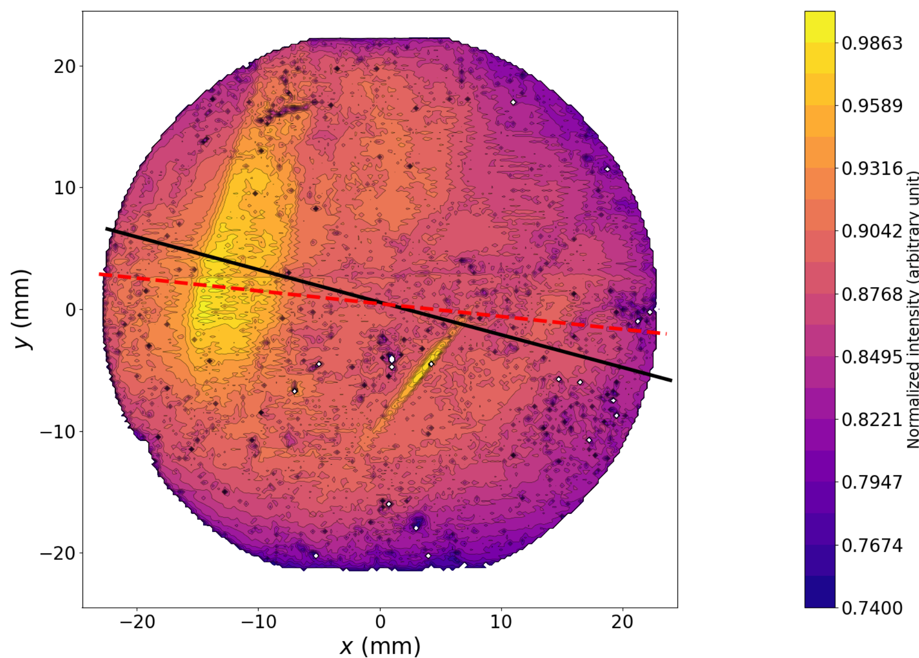

Figure 3.3: The reflection measurement of the copper sample, affected by the oxidation and dust particles, the uniformity change and RHEED line are shown, matching the transmissivity measurements. The experimentally estimated direction of the effusion cell (black line) deviating from the real direction (red dashed line) by 8°.

3.1.2 Silver

The next sample measured was silver grown on sapphire without any azimuthal rotation. By the estimate of the parameters of the effusion cell, the anticipated thickness of the film should be approximately 10,9 nanometers.

Figure 3.4 illustrates the transmission measurement of the silver, revealing a distinct structural variation compared to the previous copper sample. In this case, the upper right side of the film exhibits a higher level of transmitted light, gradually decreasing in intensity towards the left. Conversely, the reflection measurements, as depicted in Figure 3.5, yield slightly different results. Interestingly, the maximum intensity aligns with the same side observed in the transmission

measurement, suggesting that the effusion cell responsible for the flux distribution (as shown in Figure 1.8) was positioned on the upper right side of the substrate.

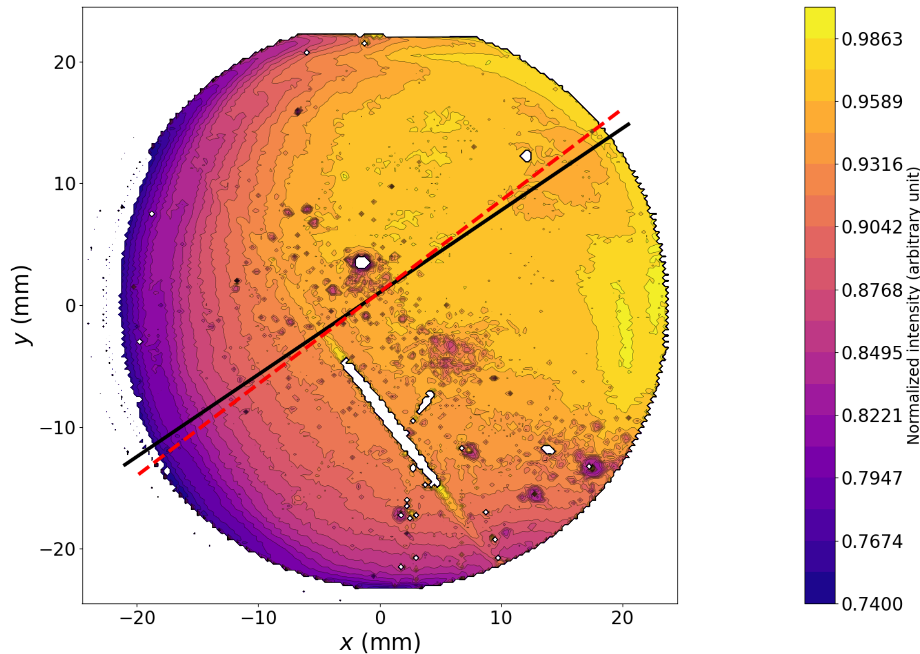

Figure 3.4: The transmission measurement of the silver sample, slightly affected by the oxidation, intensity change and RHEED line are visible. The experimentally estimated direction of the effusion cell (black line) deviating from the real direction (red dashed line) by 3,5°.

The estimated position of the effusion cell in both reflection and transmission measurements was very accurate, as depicted by the black lines, closely aligned with the red dashed lines (real geometry) in Figure 3.4 for transmission (3,5° deviation) and Figure 3.5 for reflection (9° deviation).

The observed difference in uniformity between the measurements could potentially be attributed to the oxidation of the grown film. It is important to note that all of our films were grown over a year prior to the measurement date. In Figure 3.4, there are numerous structural defects apparent, which are likely the result of oxidation affecting the silver film.

Both the transmission and reflection measurements reveal the presence of the RHEED line. However, in this particular case, the RHEED affected the measurement in a way that the line is thinner in the transmission measurement, which contrasts with the copper measurement where it was thicker.

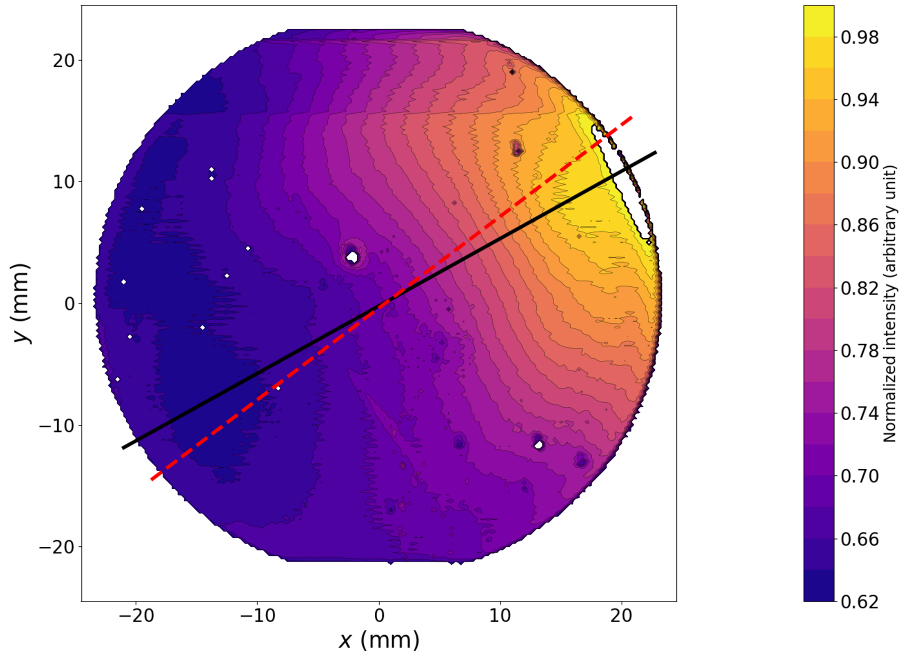

Figure 3.5: The reflection measurement of the silver sample, the change in uniformity is clearly depicted, with less visible RHEED line. The experimentally estimated direction of the effusion cell (black line) deviating from the real direction (red dashed line) by 9°.

3.1.3 Manganese

The subsequent film examined for uniformity was composed of manganese, with estimated thickness of 14,8 nanometers. It is worth noting that the manganese film exhibited significant oxidation, which posed challenges in accurately assessing its uniformity. The oxidation led to the formation of structural defects that affected the overall intensity measurements due to scattering. The presence of these defects further complicated the precise evaluation of uniformity in the manganese sample.

Figure 3.6 presents the transmitted light measurement, which reveals the prominent effects of oxidation, leading to inaccuracies in the measurement. Despite this limitation, we can still discern a noticeable change in uniformity from the bottom to the top right of the sample. This change is further supported by examining the reflection measurements (Fig. 3.7), where the impact of oxidation is less pronounced. Similarly, we observe a consistent variation in uniformity from the bottom to the top of the film. Based on the shape of the equiuniform surfaces, we can infer that the effusion cell was inclined towards the bottom side of the sample during the deposition process.

Due to the absence of a discernible RHEED line, it was not possible for us to calculate the rotation relative to the original geometry. As a result, the red dashed lines in Figures 3.6 and 3.7 represent the original non-rotated directions of the effusion cells (198° as shown in Figure 2.13). Consequently, it was not feasible to evaluate the accuracy of the direction in this case.

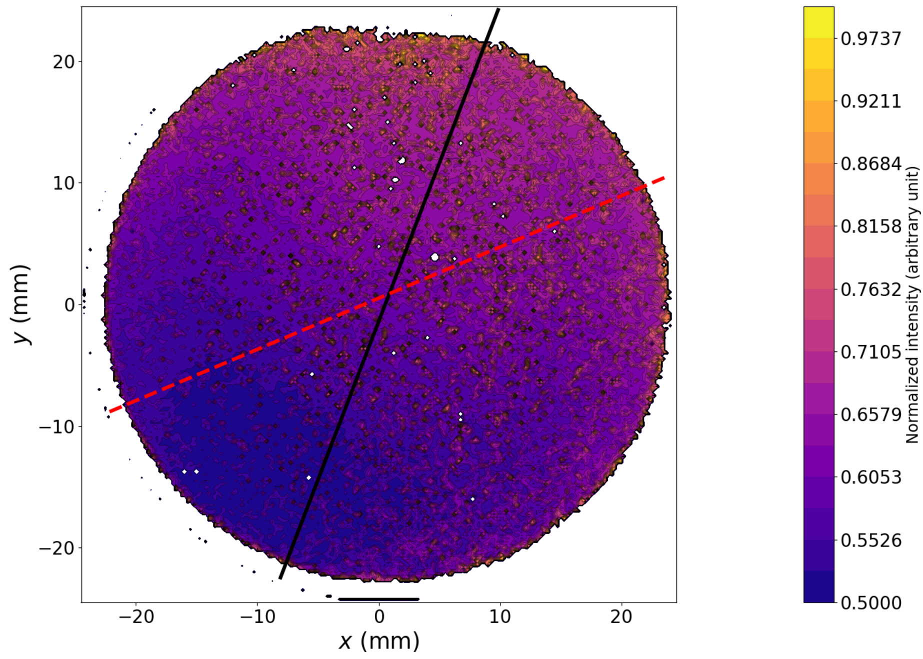

Figure 3.6: The transmission measurement of the manganese sample, visibly damaged by the oxidation, still having a noticeable change in uniformity. The experimentally estimated direction (black line) does not correspond with the real direction due to the undetermined rotation, deviating by 54°.

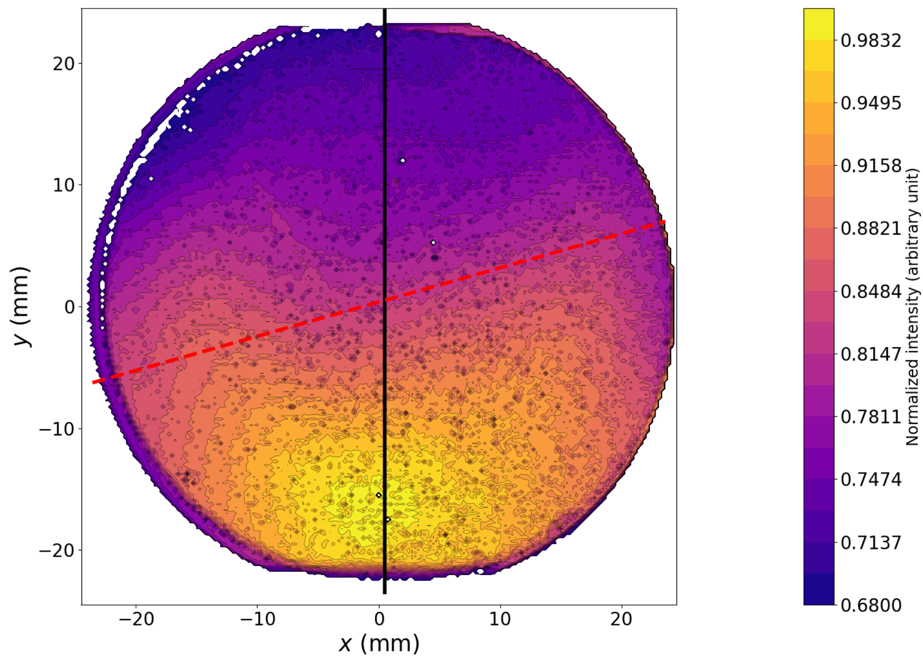

Figure 3.7: The reflection measurement of the manganese sample, the impact of oxidation is less pronounced, and a clearer change in uniformity can be seen. The experimentally estimated direction (black line) does not correspond with the real direction due to the undetermined rotation, deviating by 72°.

3.1.4 Arsenic

The sample with an arsenic-grown film, estimated to be around 45 nanometers in thickness, exhibited severe oxidation and was among the most heavily damaged samples in this regard.

In the transmission analysis, the only distinguishable feature is the presence of the RHEED line, which, similar to the silver sample, appears thinner compared to its surroundings. The extensive oxidation experienced by this sample limited our ability to observe further details or structures within the transmission analysis.

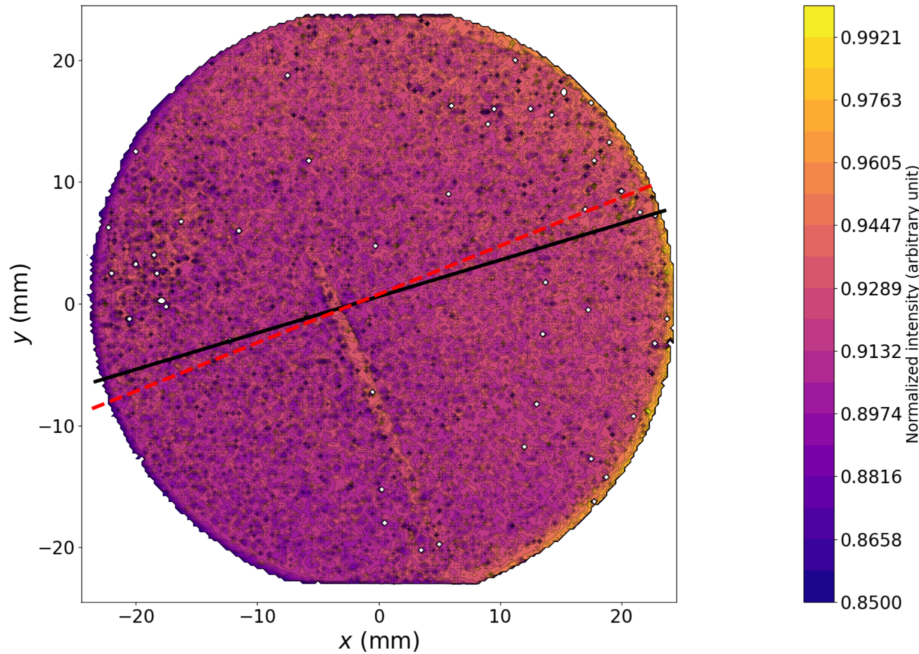

Figure 3.8: The transmission measurement of the arsenic sample, heavily damaged by the oxidation of the film, showing only a RHEED line. The experimentally estimated direction of the effusion cell (black line) deviating from the real direction (red dashed line) by 4,5°.

The reflection measurement reveals a more discernible change in uniformity, with higher intensity of reflected light on the right side gradually decreasing to lower intensity on the left side. Despite being heavily oxidized, this observation provides valuable insights into the growth process. Assuming similar conditions as in previous measurements, it can be inferred that the effusion cell was positioned on the right side of the sample, resulting in a thicker layer of arsenic that gradually thinned towards the left side.

Despite the significant oxidation of the arsenic sample, the visibility of the RHEED line allowed us to determine the rotation, enabling us to accurately estimate the direction of the effusion (black lines in Fig. 3.8 and 3.9), in both measurements deviating from real direction (red dashed lines) by only 4,5°. This precision was maintained even in the presence of heavy noise in the transmission measurement.

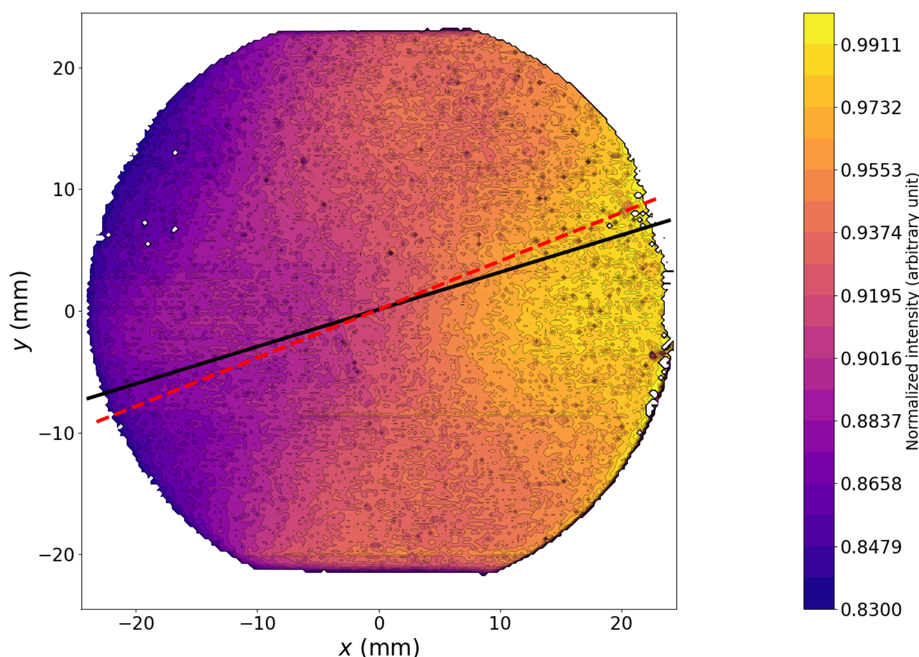

Figure 3.9: The reflection measurement of the arsenic sample, change in uniformity is more discernible. The experimentally estimated direction of the effusion cell (black line) deviating from the real direction (red dashed line) by 4,5°.

3.1.5 Gallium

The final film in our analysis was composed of gallium, which exhibited relatively lower levels of oxidation compared to the other samples. The estimated thickness of the gallium layer was approximately 16,9 nanometers.

In the transmission measurement (Fig. 3.10), a distinct and gradual change in uniformity is evident, ranging from the top right side to the bottom left side of the sample. Additionally, two residual lines resulting from the RHEED measurements are clearly visible. Notably, a significant defect is present caused by accidental contact with the sample. Since gallium has a relatively low melting point of approximately 30°C, some of the films experienced damage as a consequence.

The reflection measurement exhibits a nearly identical pattern to the transmission measurement but in an inverted form, indicating the reliability of the measurement. Additionally, two lines resulting from the RHEED measurement and a noticeable defect on the left side are observable. This sample is the only one having two lines, the upper one less prominent created by the first RHEED measurement on an empty sapphire substrate, which was subsequently rotated by the 90° and then the thin film of gallium was deposited, creating the second line, which is consistent with the samples measured before. Based on these measurements and the spatial configuration of the film, we can infer that the effusion cell was located in the top right part of the sample. Consequently, the thickest part of the film should be in that region, gradually tapering off towards the lower left.

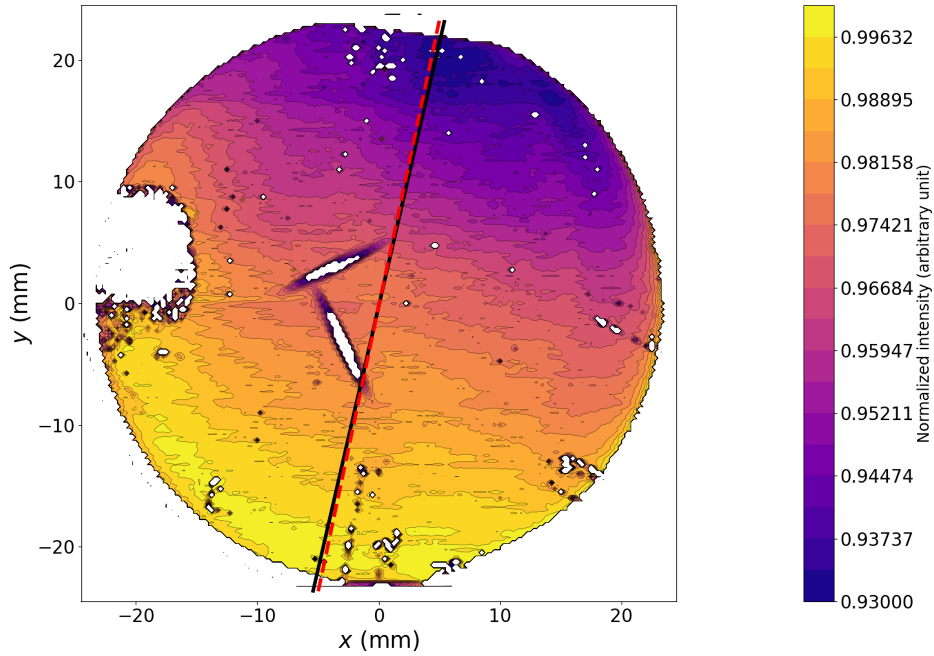

Figure 3.10: The transmission measurement of the gallium sample, containing two RHEED lines and one large defect and a small number of less significant defects. The experimental estimation of the effusion direction (black line) in almost exact agreement with the real direction (red dashed line), deviating by only 1°.

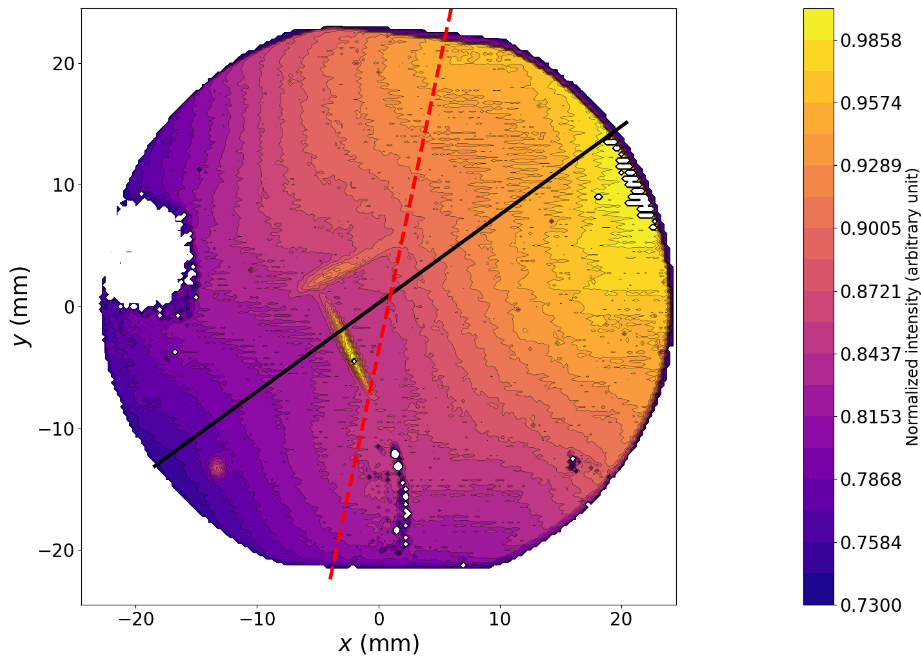

Figure 3.11: The reflection measurement of the gallium sample, containing two RHEED lines and one large defect and a small number of less significant defects, confirming the expected geometry. The experimental estimation of the effusion direction (black line) not greatly aligned with the real direction (red dashed line), deviating by 42°.

The reflection and transmission measurements exhibited disparities within

the gallium sample, potentially resulting in divergent outcomes regarding the estimation of effusion cell direction. The experimental estimation of the effusion direction through transmission measurements (depicted as the black line in Figure 3.10) displayed a closer alignment with the actual effusion direction (illustrated as the red dashed line in Figure 3.10), deviating by only 1°, in contrast to the reflection measurement, which deviated by 42° (Figure 3.11).

4. Discussion

In the previous chapter, we have pointed out some of the problems we encountered. Now, our focus will be on addressing these issues and devising effective solutions to overcome them. Additionally, we will discuss planned upgrades that can enhance the functionality and versatility of our device for future applications. These upgrades will be conducted after the finishing of this thesis since this device was built with the intent to be practically used in the future to assess the uniformity of the MBE growth.

4.1 Oxidation and Dust Pollution

The primary issue that significantly affected our measurement results was the oxidation of the samples. An image of the oxidated layer of the manganese film made by Scanning Electron Microscope (SEM) can be seen in Figure 4.1.

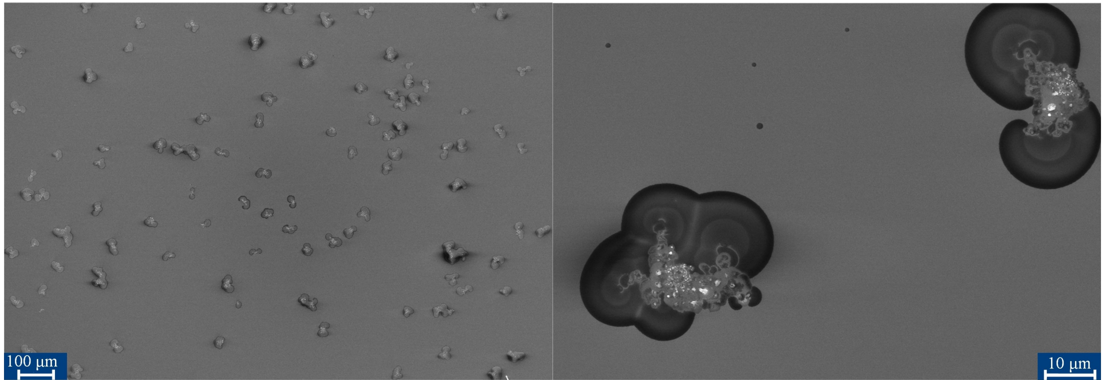

Figure 4.1: An image made by SEM of the oxidation on the manganese film.

The growth of all our samples took place in the spring of last year, making them over a year old at the time of the measurement. As a result, some of these thin films were more susceptible to oxidation, which is the most visible in the transmission measurements of arsenic (Figure 3.8).

This issue can be considered more of an unfortunate coincidence rather than a persistent problem. Moving forward, the device is anticipated to be used on freshly grown samples that are free from such defects, thus directly resolving this particular issue.

Because of significant oxidation, we encountered difficulties in conducting further analysis and accurately determining the film's thickness. Once we obtain non-oxidized samples, we will be able to integrate this aspect into the analyzing program. By utilizing known constants of the individual materials and obtaining the reference measurement of the clear substrate, it becomes feasible to accurately calculate the precise change in thickness. Incorporating this feature will significantly improve the usability of our measuring device, making it even more effective in studying thin films.

Another issue we encountered was the presence of dust particles in the air settling on the surface of the sample, causing light refraction/scattering. This issue

was particularly noticeable on the sample with a copper film (Figure 3.2), which we frequently used for measurement calibration. The dust particles disrupted our measurements and left points with abrupt changes in reflectivity/transmissivity visible in the measured data.

To address this problem, several potential solutions can be implemented. One option is to construct a protective enclosure for the device with its own air filtration, effectively blocking dust particles from contaminating the samples during measurements. Another approach would involve relocating the measurement setup to a controlled environment, such as a clean room equipped with air filters. Both of these solutions aim to minimize the presence of dust particles and mitigate their disruptive impact on the measurement process. Considering that our laboratory also includes rooms with filtered air, the second option would be the preferred choice.

4.2 Device Improvements

Within this section, we will discuss the planned upgrades to increase user comfort while using our device. We devised these upgrades from our experience of using the device during the measurements conducted in the scope of this thesis.

4.2.1 Samples on Different Substrates

Given that our device incorporates modular design, we have the flexibility to substitute certain parts of the device without affecting other functions. This capability enables us to expand the range of samples we can measure or add new functionality.

One potential approach to enhance versatility is by substituting the red laser diode with an infrared or a different wavelength that operates in the transparency region of the used substrate with measured film, enabling the laser beam to pass through the substrate without absorption. Additionally, the detectors can also be changed if necessary to cover the broader spectrum than 200 to 1100 nm of our current Si detectors, depending on the situation's requirements. This modification will enable the analysis of different films.

Our device is equipped with a removable 3D printed sample holder that offers flexibility for modification. By adapting and customizing the sample holder, it becomes possible to accommodate a wide range of sample sizes and types.

4.2.2 Compactness

Despite its small size, operating our device requires complex readout electronics, such as a lock-in amplifier and a signal generator. However, when considering these components together, they are considerably larger than the device itself, thereby limiting its compactness. To address this issue, one potential solution is to replace these two components with a National Instruments Data Acquisition (DAQ) card, which can act as a signal generator for the laser diode and digital lock-in amplifier for the photodiode readout. By employing a measuring card, we can significantly reduce the overall size of the setup while still maintaining the necessary functionality for accurate measurements. Due to time constraints and

the complex nature of implementing this card, we were unable to add it to our setup in time.

Incorporating the measuring card into our device offers multiple advantages. Not only does it reduce the overall size, but it also enables simultaneous measurement of transmissivity and reflectivity. The size constraints of our previous setup limited us to connecting only one lock-in amplifier, restricting data collection to a single detector. However, with the measuring card, we can gather data from multiple detectors simultaneously.

Furthermore, our setup includes a programmable function generator that generates sine waves. However, this component can also be replaced with a smaller power amplifier connected to the DAQ card or by a purpose-built standalone function generator set to a distinct frequency. By utilizing either alternative, we can further reduce the overall size of the setup without compromising the required frequency functionality.

4.2.3 User Experience

Throughout our measurements, we encountered the inconvenience of relying on a laptop computer to control the measurement process and perform data analysis. It required manually modifying the code for each measurement, which proved to be impractical for experimental purposes.

To address this issue and enhance the measurement process, it is crucial to automate the configuration process by eliminating the need to manually change the code. A viable solution would involve incorporating a user-friendly Graphical User Interface (GUI) to manage the measurements. This approach would streamline the measurement procedure by separating user interaction from the complexities of the underlying code, thereby simplifying the overall operation. With the GUI, users would only need to set the desired measurement parameters, while the system takes charge of executing the sample measurement and subsequent evaluation.

By adopting this automated and GUI-driven methodology, our measuring device would undergo a significant transformation, becoming a highly convenient and efficient tool for measuring uniformity. This upgrade would not only save time and effort but also enhance the usability of the device, making it more accessible to a wider range of users within our laboratory setting.

Conclusion

A specialized machine, specifically designed and constructed to analyze the impact of asymmetry in an MBE machine on the uniformity of samples, was designed and constructed. This machine facilitated the examination of various samples through transmissivity and reflectivity measurements.

The samples used in our measurements were over a year old, resulting in the presence of oxidation layers, particularly noticeable in the arsenic and manganese samples. In these measurements, the reflection measurement proved to be more reliable as it reflected from the bottom side of the film through a substrate, where the interface was kept from oxidizing. Consequently, for evaluation purposes, we relied mainly on the reflection measurements. Comparing the results with the other measurements, we were able to estimate the asymmetric position of the effusion cell.

In contrast, the set of samples consisting of copper, gallium, and silver exhibited significantly less oxidation. This allowed us to compare both the transmission and reflection measurements more effectively, enabling us to estimate the position of the effusion cell better.

Due to the prolonged exposure of the copper sample used for device calibration, it remained in an open space for an extended period, resulting in visible marks caused by dust particles in the measurement data. Unfortunately, these particles had a detrimental impact on the accuracy of our results, leading to a degradation in the quality of the measurements.

Furthermore, in all of the samples, except for manganese, we observed remnants of a line after the RHEED measurement. This line disrupted the overall uniformity of the film, causing an undesired variation that was unrelated to the uniformity of a molecular beam.

Nevertheless, during the analysis phase, we successfully created a script that was able to identify and mitigate the majority of unwanted irregularities, which complicated our analysis. This enabled us to visualize the data, determine the uniformity of the films, and also to find the points of maximum and minimum intensity that helped us to assess the parameters of the MBE system.

Bibliography

[1] Marian A Herman and Helmut Sitter. *Molecular beam epitaxy*. Springer Series in Materials Science. Springer, Berlin, Germany, December 1989.

[2] K. Alavi. Molecular beam epitaxy. In *Encyclopedia of Materials: Science and Technology*, pages 5765–5780. Elsevier, 2001.

[3] Karl Jousten, Jürgen Dirscherl, Rudolf Lachenmann, Alfons Jünemann, Ing. Friedrichsen, Erik Lippelt, and Ing. Boris Kossek. Positive displacement pumps. In *Handbook of Vacuum Technology*, pages 259–360. Wiley-VCH Verlag GmbH & Co. KGaA, July 2016.

[4] Fouad G Major, Viorica N Gheorghe, and Gunther Werth. *Charged particle traps*. Springer Series on Atomic, Optical, and Plasma Physics. Springer, Berlin, Germany, 2005 edition, October 2004.

[5] C.T. Foxon, M.R. Boudry, and B.A. Joyce. Evaluation of surface kinetic data by the transform analysis of modulated molecular beam measurements. *Surface Science*, 44(1):69–92, July 1974.

[6] A J SpringThorpe. Mass spectrometry during molecular-beam epitaxy: An alternative to reflection high-energy electron diffraction. *J. Vac. Sci. Technol. B Microelectron. Nanometer Struct. Process. Meas. Phenom.*, 6(2):754, March 1988.

[7] A. Y. Cho. Film deposition by molecular-beam techniques. *Journal of Vacuum Science and Technology*, 8(5):S31–S38, September 1971.

[8] J. H. Neave, B. A. Joyce, P. J. Dobson, and N. Norton. Dynamics of film growth of GaAs by MBE from rheed observations. *Applied Physics A Solids and Surfaces*, 31(1):1–8, May 1983.

[9] M D Pashley, K W Haberern, W Friday, J M Woodall, and P D Kirchner. Structure of GaAs(2 x 4)-c(2 x 8) determined by scanning tunneling microscopy. *Phys. Rev. Lett.*, 60(21):2176–2179, May 1988.

[10] R F Bunshah, editor. *Techniques involving extreme environment, nondestructive techniques, computer methods in metals research and data analysis: Pt. 2*. Techniques of Metals Research S. John Wiley & Sons, Nashville, TN, December 1976.

[11] B Bölger and P K Larsen. Video system for quantitative measurements of RHEED patterns. *Rev. Sci. Instrum.*, 57(7):1363–1367, July 1986.

[12] J. Marquis, K. Roodenko, P. Pinsukanjana, and W. Frensley. Development of a long-wave infrared band-edge (lwir be) thermometry instrument. *Review of Scientific Instruments*, 89(7):074903, 2018.

[13] P A Maki, S C Palmateer, A R Calawa, and B R Lee. Elimination of flux transients in molecular beam epitaxy. *J. Electrochem. Soc.*, 132(11):2813–2814, November 1985.

[14] John Orton Charles, John Orton, and Charles Thomas Foxon. *Molecular beam epitaxy*. Oxford University Press, Cary, NC, January 2015.

[15] Irving Langmuir. The vapor pressure of metallic tungsten. *Physical Review*, 2(5):329–342, November 1913.

[16] Martin Knudsen. Die gesetze der molekularströmung und der inneren reibungsströmung der gase durch röhren. *Ann. Phys.*, 333(1):75–130, 1909.

[17] Marian A Herman. Physical problems concerning effusion processes of semiconductors in molecular beam epitaxy. *Vacuum*, 32(9):555–565, January 1982.

[18] J. Humenberger and H. Sitter. Study of thermodynamic processes in the hot wall reactor for the growth of high quality cdte on gaas. *Thin Solid Films*, 163:241–247, 1988.

[19] W. Gericke, M. Höricke, and J. von Kalben. A detailed study of the molecular beam flux distribution of mbe effusion sources. *Vacuum*, 42(18):1209–1212, 1991.

[20] Prasanta Kumar Basu, Bratati Mukhopadhyay, and Rikmantra Basu. *Semiconductor Laser Theory*. CRC Press, Boca Raton, FL, June 2015.

[21] Eduard Belas and Pavel Moravec. Fotonové detektory záření. `http://fu.mff.cuni.cz/semicond/media/files/courses/detekce6_714ODRn.pdf`. Accessed: 28-06-2023.

[22] Max Born and Emil Wolf. *Principles of optics*. Cambridge University Press, Cambridge, England, 7 edition, October 1999.

[23] Mingzhou Yin, Yue Chen, Kit-Hang Lee, Denny K.C. Fu, Zion Tsz Ho Tse, and Ka-Wai Kwok. Dynamic modeling and characterization of the coreXyCartesian motion system. In *2018 IEEE International Conference on Real-time Computing and Robotics (RCAR)*. IEEE, August 2018.

[24] Gaussovské svazky. `https://physics.mff.cuni.cz/kchfo/ooe/pdf/praktika_gauss.pdf`. Accessed: 20-05-2023.

[25] Charlotte Bond, Daniel Brown, Andreas Freise, and Kenneth A. Strain. Interferometer techniques for gravitational-wave detection. *Living Reviews in Relativity*, 19(1), December 2016.

[26] The measurement of a transverse profile of laser beam by knife edge method. `https://people.fjfi.cvut.cz/blazejos/public/ul7en.pdf`. Accessed: 20-05-2023.

List of Figures

1.1 Schematic representation of the key components within an MBE growth machine. Adapted from [2]. 5
1.2 Gas path in scroll pump. Adapted from [3]. 6
1.3 Schematic representation of ion-getter pump. 7
1.4 Basic structure of a cryopump. 7
1.5 Schematic diagram illustrating the RHEED geometry. It showcases the incident beam positioned at an angle θ relative to the surface plane, along with the azimuthal angle ϕ. The elongated spots within the diagram represent the points of intersection between the Ewald sphere and the 01, 00, and $0\bar{1}$ rods. Adapted from [11]. 9
1.6 A schematic illustration depicting the upper section of an ideal Knudsen effusion cell. The diagram highlights the geometric quantities that are relevant to the calculations of flux distribution. Adapted from [1]. 12
1.7 Molecular flux distribution across axially (a) and non-axially (b) mounted substrates, in relation to the effusion cell orifice in the MBE chamber. Adapted from [17]. 13
1.8 Density of particles crossing the exit of the hot-wall tube (a) and density of particles impinging on a plane positioned at a distance L/R above the tube opening(b). Adapted from [18]. 14
1.9 The thickness distributions from the cylindrical and conical crucibles under the conditions of $T = 630°C$ and $L/R = 2$. Adapted from [19]. 14
1.10 The interaction of radiation with a two-level atomic system with three fundamental processes: (a) absorption, (b) spontaneous emission, and (c) stimulated emission. Each process represented by a diagram where the left half depicts the initial state of occupancy of a level, and the right half represents the state of occupancy after the process. Adapted from [20]. 15
1.11 The EM field distribution of three longitudinal modes within a Fabry-Perot resonator. Adapted from [20]. 17
1.12 (a) basic Si photodiode structure (b) V-A characteristic of a photodiode, Φ_0, Φ_1 and Φ_2 being the photon fluxes, i_0 the dark current, i_λ the photocurrent, $i_{k1;2}$ the reverse saturation current and $V_{P1;2}$ the output voltage. Adapted from [21]. 19
1.13 (a) Schematic of a photodiode: (a): two possible connections PV mode (1) and PC mode (2). J_λ current generated by the incident light, R_{Sh} parallel resistance, R_S serial resistance, C_d parallel capacitance, R_L working resistance, (b) schematic of the photodiode in the PC mode: (1) the depletion region, (2) drifting region (3) electron and hole diffusion region. Adapted from [21]. 20
1.14 Spectral current sensitivity of photodiode dashed line showing the theoretical curve according to (1.26), continuous line showing the real photodiode, λ_g depicting the long-wavelength cutoff. Adapted from [21]. 20

1.15 Propagation of an electromagnetic wave through a homogenous dielectric film, consisting of three dielectric media labeled 1,2,3, with corresponding refraction indexes n_j. θ_j marking the incident and transmitted angles, h the height of the second medium ($j = 1, 2, 3$). Adapted from [22]. 22
1.16 An absorbing film situated between two dielectric media, divided into three parts labeled 1,2,3. 1 and 3 being dielectric, while 2 being a conductor with corresponding refraction indexes n_1, n_3 and $\hat{n}_2$ (hat indicating absorbing medium), θ_j marking the incident and transmitted angles, h the height of the second medium ($j = 1, 2, 3$). Adapted from [22]. 24
1.17 The reflectivity $\mathcal{R}$ and transmissivity $\mathcal{T}$ of a metallic film as functions of its optical thickness for normal incidence. $[n_1 = 1; n_2 = 3,5; n_3 = 1,5; \kappa_1 = \kappa_3 = 0; \theta_1 = 0]$ Adapted from [22]. 27

2.1 The setup without the aluminum skeleton and core-xy movement system. 28
2.2 Schematics of Core-XY system, two belts (in red and blue) connected with the ample holder at four points symmetrically. Components 1 and 2 are the stationary driving units at four points symmetrically. Components 3-10 are the idle pulleys. Adapted from [23]. 30
2.3 3d model of the core-xy system. 30
2.4 2-inch sample divided into 0,5 mm long squares, the blue dots show the centers of the squares. 31
2.5 The measurement of long-term continuous laser stability with detectors directly connected to the voltmeter. 32
2.6 The measurement of long-term continuous laser stability with a lock-in amplifier added between the detector and voltmeter. . . . 33
2.7 A typical pattern displaying the intensity of a laser beam (left) and the distributions of intensity and amplitude for a normalized Gaussian beam (right). Adapted from [25]. 34
2.8 Schematic of a Knife Edge method. Adapted from [26]. 34
2.9 Example of the measured and fitted data using the knife-edge method in y direction. 35
2.10 Comparison of the first derivative and fit of 2.9. 35
2.11 Basic colormap of the measured Gallium on Sapphire substrate. . 36
2.12 The improved colormap with removed irregularities and edge of the sample. 37
2.13 The internal geometry of effusion cells and RHEED in an MBE machine. 38
2.14 The improved colormap with a red dashed line depicting the real direction of the effusion cell and a black line, depicting the experimentally estimated direction. 38

3.1 The transmission measurement of the clear substrate, the accuracy of the measurements and the effects of the lock-in noise are shown. 40

3.2 The transmission measurement of the copper sample, affected by the oxidation and dust particles, the uniformity change and RHEED line are clearly visible. The experimentally estimated direction of the effusion cell (black line) deviating from the real direction (red dashed line) by 9°. 41
3.3 The reflection measurement of the copper sample, affected by the oxidation and dust particles, the uniformity change and RHEED line are shown, matching the transmissivity measurements. The experimentally estimated direction of the effusion cell (black line) deviating from the real direction (red dashed line) by 8°. 42
3.4 The transmission measurement of the silver sample, slightly affected by the oxidation, intensity change and RHEED line are visible. The experimentally estimated direction of the effusion cell (black line) deviating from the real direction (red dashed line) by 3,5°. 43
3.5 The reflection measurement of the silver sample, the change in uniformity is clearly depicted, with less visible RHEED line. The experimentally estimated direction of the effusion cell (black line) deviating from the real direction (red dashed line) by 9°. 44
3.6 The transmission measurement of the manganese sample, visibly damaged by the oxidation, still having a noticeable change in uniformity. The experimentally estimated direction (black line) does not correspond with the real direction due to the undetermined rotation, deviating by 54°. 45
3.7 The reflection measurement of the manganese sample, the impact of oxidation is less pronounced, and a clearer change in uniformity can be seen. The experimentally estimated direction (black line) does not correspond with the real direction due to the undetermined rotation, deviating by 72°. 45
3.8 The transmission measurement of the arsenic sample, heavily damaged by the oxidation of the film, showing only a RHEED line. The experimentally estimated direction of the effusion cell (black line) deviating from the real direction (red dashed line) by 4,5°. . . . 46
3.9 The reflection measurement of the arsenic sample, change in uniformity is more discernible. The experimentally estimated direction of the effusion cell (black line) deviating from the real direction (red dashed line) by 4,5°. 47
3.10 The transmission measurement of the gallium sample, containing two RHEED lines and one large defect and a small number of less significant defects. The experimental estimation of the effusion direction (black line) in almost exact agreement with the real direction (red dashed line), deviating by only 1°. 48
3.11 The reflection measurement of the gallium sample, containing two RHEED lines and one large defect and a small number of less significant defects, confirming the expected geometry. The experimental estimation of the effusion direction (black line) not greatly aligned with the real direction (red dashed line), deviating by 42°. 48

4.1 An image made by SEM of the oxidation on the manganese film. . 50

List of Abbreviations

AES Auger Electron Spectroscopy. 4, 8

ARC Anti-Reflective Coating. 29, 30

BET Band-Edge Thermometry. 9

CGS Centimetre–gram–second system. 11, 13

CNC Computer Numerical Control. 29, 32

DAQ Data Acquisition. 51, 52

EM electromagnetic. 15, 19

GUI Graphical User Interface. 52

HV High Vacuum. 5

IGP Ion-Getter Pump. 6

IR Infrared. 9

MBE Molecular Beam Epitaxy. iii, 3–6, 8, 9, 13, 38, 40, 50, 53, 56, 57

MBMS Modulated Beam Mass Spectroscopy. 8

PC Photoconductive. 19, 20, 56

PV Photovoltaic. 18–20, 56

RHEED Reflection High Energy Electron Diffraction. 4, 8, 9, 36, 38, 41–44, 46–48, 53, 56–58

SEM Scanning Electron Microscope. 50, 59

TE Transverse Electric. 21, 23–26

TM Transverse Magnetic. 21, 22, 25–27

UHV Ultra-High Vacuum. 4–6, 8, 11